Freie Universität Berlin

FRITZ-HABER-INSTITUT
MAX-PLANCK-GESELLSCHAFT

Master Thesis in Chemistry

High-resolution UV spectroscopy of 1-phenylethanol

Written By

Shilpa Yadav

Matriculation No: 5570286

Supervisor

Dr. Sandra Eibenberger-Arias

Fritz-Haber-Institut der Max-Planck-Gesellschaft

First Examiner

Prof. Dr. Gerard Meijer

Fritz-Haber-Institut der Max-Planck-Gesellschaft

Second Examiner

Prof. Dr. Kevin Pagel

Freie Universität Berlin

Submitted on

16.05.2024

-

Declaration

I, **Shilpa Yadav**, hereby declare that the master's thesis entitled High-resolution UV spectroscopy of 1-phenylethanol submitted in fulfillment of the requirements for the Master of Science degree in Chemistry at Freie Universität Berlin is my original work unless otherwise indicated. I confirm that: 1. I conducted my own independent research and investigation for this thesis, and I have properly cited and acknowledged all sources, whether directly quoted or paraphrased, in the bibliography. 2. The acknowledgments section appropriately acknowledges any assistance I received in preparing this thesis, including contributions from colleagues and guidance from advisors. 3. This thesis has not been submitted for any other degree or qualification at any other university or institution. Any violation of academic integrity or misrepresentation of authorship in this thesis could lead to serious consequences, including the revocation of the degree I received.

Berlin, 16/05/2024

Abstract

Chiral molecules are of considerable interest across various fields of science, particularly due to their pivotal role in pharmaceuticals and biological processes. Over recent decades, spectroscopic techniques for chiral analysis have developed. Among these, the enantiomer-specific state transfer (ESST) method has emerged as a standout approach. Based on microwave (MW) spectroscopy, ESST facilitates chiral separation in different rotational states. Recent advancements of this method incorporate ultraviolet (UV) radiation into ESST to improve the transfer efficiency, which necessitates a precise understanding of the distinct rotational energy level structures in both the ground and the first electronically excited state of the target molecules.

Building on this need, this thesis presents a comprehensive high-resolution UV spectroscopic study of 1-phenylethanol, a potential target molecule for ESST studies. Using a jet-cooled pulsed molecular beam, we performed vibrationally and rotationally resolved UV spectroscopy through resonance-enhanced multiphoton ionization (REMPI) and laser-induced fluorescence (LIF), respectively. Our work aimed to characterize the rotational energy level structure of 1-phenylethanol in the first electronically excited state.

We recorded a vibrationally resolved REMPI spectra of the $S_1 \leftarrow S_0$ electronic transition using a pulsed dye laser. Through comparisons with theoretical one-photon absorption calculations, we identified the origin band and additional vibrational features in the spectrum. Additionally, we determined the lifetime of the S_1 state to be 70 ns using two time-delayed pulsed lasers, corresponding to a natural linewidth of 2.2 MHz

Subsequently, a rotationally resolved spectrum of the origin band of the $S_1 \leftarrow S_0$ electronic transition, initially identified using REMPI, was recorded via LIF detection. The linewidth of the spectrum was measured to be 54 MHz, suggesting that Doppler broadening is a significant factor affecting the observed spectral linewidth. The measured spectrum was analyzed using the PGOPHER software. Starting with known and calculated rotational constants, we refined the fit to the measured data to accurately determine the rotational constants of the S_1 state. These parameters provide a detailed understanding of the rotational energy level structure, which is essential for potential applications in ESST.

Acknowledgements

I would like to express my sincere gratitude to my supervisor, Dr. Sandra Eibenberger-Arias, for her invaluable guidance, unwavering support, and insightful feedback throughout this research. Her constant availability and the opportunity to work on this project are deeply appreciated.

I am grateful to Prof. Dr. Gerard Meijer for his continued guidance and to Prof. Dr. Kevin Pagel for their willingness to review and evaluate this thesis.

My heartfelt thanks go to my colleagues: JuHyeon Lee for her diligent review and feedback on my thesis, as well as her constant motivation and guidance; Elahe Abdiha for her motivational support and assistance in writing this thesis; and Nadia González for her help in the laboratory. I also thank Dr. Boris Sartakov, Daniel Barroso, and Russell Thomas for their valuable support throughout this process.

Finally, I extend my deepest gratitude to my family and friends, especially Kunal, for their unwavering support and encouragement throughout my studies. I am also grateful for God's grace, which has made this journey both enriching and enjoyable.

Contents

List of Figures

List of Tables

Acronyms

ESST: Enantiomer-Specific State Transfer

MW: Microwaves

UV: Ultraviolet

REMPI: Resonance-Enhanced Multiphoton Ionization

LIF: Laser-Induced Fluorescence

DFT: Density Functional Theory

TD-DFT: Time Dependent Density Functional Theory

IR: Infrared

TOF-MS: Time of Flight Mass Spectrometer

LDA: Local Density Approximation

GGA: Generalized Gradient Approximation

LR-TDDFT: Linear-Response TDDFT

B3LYP: Becke, 3-parameter, Lee–Yang–Parr

Nd-YAG: Neodymium-Yttrium Aluminum Garnet

KDP: Potassium Dihydrogen Phosphate

MCP: Microchannel Plate Detector

HR: High-Resolution

FWHM: Full Width at Half Maximum

PMT: Photomultiplier Tube

PES: Potential Energy Surface

AH: Adiabatic Hessian Model

CW: Continuous-Wave

CHAPTER 1

Introduction

A chiral molecule cannot be perfectly overlapped with its mirror image, leading to the formation of two distinct forms known as enantiomers. Although these enantiomers share almost identical physical properties, their interactions with other chiral molecules differ significantly. Many biomolecules are chiral and exist in only one form of handedness, a phenomenon termed homochirality.[1] This specificity in molecular orientation is crucial in biological processes and pharmaceutical applications. The thalidomide tragedy underscores the importance of understanding chiral interactions in pharmaceuticals. Initially prescribed to pregnant women to alleviate morning sickness, thalidomide was subsequently discovered to have a teratogenic enantiomer, causing severe birth defects, while its mirror image enantiomer is sedative.[2] Thus, understanding the behavior and properties of chiral molecules is essential.

Over the past decades, new types of spectroscopic methods for chiral analysis have been developed. Our group specifically employs enantiomer-specific state transfer (ESST), a recently developed method that facilitates chiral separation at the quantum level.[3] This method utilizes tailored microwave (MW) fields to selectively populate or depopulate rotational states with a chosen enantiomer. Initially, the transfer efficiency of ESST was constrained by the spatial degeneracy of rotational states[4,5] and the thermal population of these states.[6] To overcome these challenges, our group developed a new spectroscopic approach that integrates ultraviolet (UV) radiation with ESST, significantly enhancing its efficiency.[7–9] This scheme enabled the first quantitative study of ESST[7] and near-perfect transfer efficiency, thereby unlocking the full potential of ESST.[9]

The selection of a suitable target molecule is critical for our specific technical implementation of ESST. The ideal molecule for our study should be chiral in C_1 symmetry[10], possess a UV chromophore, and be suitable for gas-phase studies. Furthermore, the rotational energy level structure in both ground and first excited electronic states should be previously characterized. In this thesis, we focus on 1-phenylethanol as a potential target chiral molecule for ESST. 1-Phenylethanol is a relatively simple and rigid aromatic alcohol composed of a phenyl ring bonded to an ethanol moiety (-$CHOHCH_3$). While 1-phenylethanol meets most of our criteria, its rotational energy structure in the first

electronically excited state (S_1) had not yet been studied. To address this need, we conducted high-resolution UV spectroscopy of 1-phenylethanol.

Our spectroscopic studies indicate that the most stable conformer of 1-phenylethanol predominates in the jet-cooled pulsed molecular beam, which aligns with previous research findings.[11] A vibrationally resolved resonance-enhanced multiphoton ionization (REMPI) spectra of the $S_1 \leftarrow S_0$ electronic transition was recorded using a pulsed dye laser. Through comparisons with theoretical one-photon absorption calculations, we identified the origin band and additional vibrational features. Subsequently, a rotationally resolved UV spectrum over the origin band of the same electronic transition was obtained via laser-induced fluorescence (LIF) using a continuous-wave UV laser. This spectrum was analyzed using PGOPHER, providing us with the rotational level structure of the S_1 excited state. Furthermore, the lifetime of the S_1 state has been measured using a two-color REMPI delay scan.

CHAPTER 2

Fundamental

This chapter introduces high-resolution UV spectroscopy, focusing on the line strength factors governing vibrational and rotational transitions within a specific electronic transition. A brief overview of rotational and vibrational spectroscopy is provided, followed by the principles of the REMPI and LIF techniques employed in this thesis. Finally, the computational methods of density functional theory (DFT) and time-dependent functional theory (TD-DFT) used for Gaussian calculations are outlined.

2.1 | High-resolution UV spectroscopy

UV spectroscopy is a powerful analytical tool,[12] utilizing light within the UV or visible region with wavelengths ranging from 200 to 800 nm. When a molecule absorbs a UV photon whose energy matches the difference between its electronic states, an electron transitions from a lower electronic state to a higher electronic state.[13] This electronic transition is often accompanied by changes in the vibrational and rotational states of a molecule, resulting in vibrational and rotational transitions as depicted in Fig. 2.1. High-resolution UV spectroscopy enables the resolution of these vibrational or rotational states within electronic transitions, depending on the light source's resolution. This thesis focuses on both the vibrationally and rotationally resolved $S_1 \leftarrow S_0$ electronic transition in 1-phenylethanol. The following sections discuss the factors that determine the line strength of these vibrational and rotational transitions.

2.1.1 Line strength

Under the Born-Oppenheimer approximation,[14] which decouples the nuclear and electronic motions, the total wave function of a molecule can be separated into electronic (Ψ_E), vibrational (Ψ_V), and rotational (Ψ_R) components*:

$$\Psi_{total} = \Psi_E \Psi_V \Psi_R, \tag{2.1}$$

*All the notations of the equations are adopted from the book "Angular momentum: Understanding spatial aspects in chemistry and physics" by Richard N. Zare.[15]

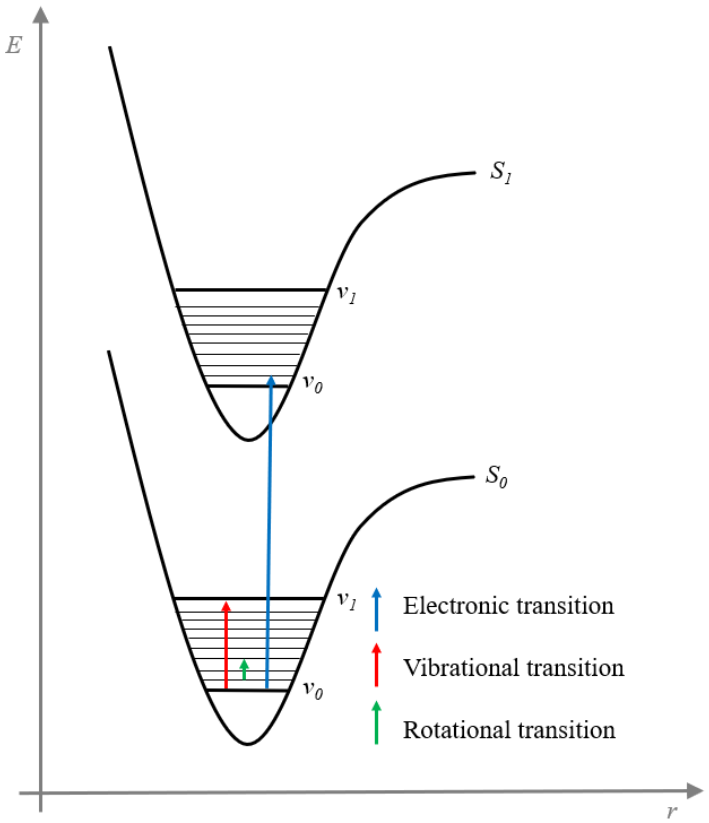

Fig. 2.1. Potential energy curves of a diatomic molecule for the ground electronic state (S_0) and an excited electronic state (S_1). The internuclear distance (r) is shown on the horizontal axis, and the potential energy (E) is on the vertical axis. Blue arrows depict electronic transition between the electronic states, while red arrows represent vibrational transition, and rotational transition is depicted by green arrow.

In rigid molecules, interactions between rotational and vibrational motions are often negligible, allowing for the separation of line strength contributions from each component:

$$S^{tot} = S^{EV} S^{R}, \tag{2.2}$$

where S^{EV} is the line strength of the $S_1(\nu') \leftarrow S_0(\nu'')$ vibronic band and S^R is the rotational line strength.

For a vibronic band, the line strength can be given by

$$S^{EV} = |\langle V'| D_{E'E''} |V''\rangle|^2. \tag{2.3}$$

$D_{E'E''}$ is constant for the $S_1 \leftarrow S_0$ transition, and the equation simplifies to:

$$S^{EV} = D^2_{E'E''} |\langle V'|V''\rangle|^2 = D^2_{E'E''} \prod_k q_{v'_k v''_k}, \tag{2.4}$$

where

$$q_{v'_k v''_k} = |\langle \psi_{v'_k} | \psi_{v'_k} \rangle|^2 \tag{2.5}$$

is known as the Franck-Condon factor for the normal mode k, which accounts for the overlap between the vibrational wavefunctions of the initial and final states.
For a rotational transition, the line strength is given by:

$$S^R = \langle R' | \mu | R'' \rangle , \tag{2.6}$$

where μ denotes the electric dipole moment and is referred to as the Hönl-London factor.

The analysis of high-resolution UV spectra of the $S_1 \leftarrow S_0$ transition in this study, relies on both the Franck-Condon and Hönl-London factors, along with the Boltzmann distribution. For the vibrationally resolved REMPI spectra, the Franck-Condon factors play a crucial role in interpreting the vibrational transitions whereas for the rotationally resolved LIF spectra, the Hönl-London factor is fundamental in analyzing the rotational transitions. To deepen our understanding of these rotational and vibrational transitions, the following sections will provide a comprehensive overview of both rotational and vibrational spectroscopy.

2.1.2 Rotational spectroscopy

Rotational spectroscopy, also known as microwave spectroscopy, is a valuable technique for elucidating the molecular structures of gas-phase molecules. It provides detailed insights into structural parameters and molecular conformations.

The moment of inertia (I) is a property of a rigid body that indicates the amount of torque required for rotational motion around an axis. It is calculated using the following formula:[16]

$$I = \sum m_i r_i^2, \tag{2.7}$$

where m_i represents the mass of each particle in the body, and r_i is the distance of each particle from the axis of rotation. The moment of inertia plays a crucial role in understanding the rotational dynamics of molecules. For any molecule, there exists a set of three mutually perpendicular axes known as the principal axes of inertia, labeled a, b, and c. By convention, the c-axis is aligned with the axis along which the moment of inertia reaches its maximum value, while the a-axis aligns with the axis where the moment of inertia is at its minimum:

$$I_c \geq I_b \geq I_a. \tag{2.8}$$

For a rigid molecule with no net orbital and spin angular momentum, the classical expression for the rotational energy is given by:[17]

$$E = \frac{J_a^2}{2I_a} + \frac{J_b^2}{2I_b} + \frac{J_c^2}{2I_c}, \tag{2.9}$$

where J_a, J_b, and J_c are the classical angular momenta along the principal molecular axes, and A, B, and C represent the rotational constants, defined by:

$$A = \frac{\hbar^2}{2I_a}, \quad B = \frac{\hbar^2}{2I_b}, \quad C = \frac{\hbar^2}{2I_c} \tag{2.10}$$

Molecules can be categorized into several types based on their principal moments of inertia: linear, spherical top, symmetric top, and asymmetric top. This section will explore linear, symmetric, and asymmetric tops, with a particular focus on asymmetric top molecules. The rotational energy levels for each type of molecule within the rigid rotor approximation are outlined below.

Linear molecules All the atoms in linear molecules lie along a single axis, with $I_a = 0$ and $I_b = I_c$. Therefore, the rotational energy for a linear molecule is described as:

$$E = BJ(J+1) \tag{2.11}$$

Symmetric top molecules For a rigid symmetric top, all three moments of inertia are non-zero, and two are identical. These can be categorized into two shapes based on their geometrical properties:

- **Prolate tops:** $I_a < I_b = I_c$ (cigar-shaped).
- **Oblate tops:** $I_a = I_b > I_c$ (disk-shaped).

The rotational energy level of a symmetric top molecule is expressed as:

$$E_{Prolate} = BJ(J+1) + (A-B)K^2, \tag{2.12}$$

$$E_{Oblate} = AJ(J+1) + (C-A)K^2. \tag{2.13}$$

where K is the quantum number representing the projection of the total angular momentum (J) onto the molecule's principal symmetry axis, with allowed values ranging from $-J$ to $+J$.

Asymmetric top molecules

The moments of inertia for a asymmetric top molecule fulfill the inequality:$I_a \neq I_b \neq I_c$. Although the energy levels are not defined by simple expressions, as they are for the other classes of molecules, the equations describing their energies are known, and the Hamiltonians can be numerically solved.[18] Furthermore, the K quantum number fails to adequately describe the rotational energy levels of asymmetric tops. This is because the K component of the angular momentum fails to remain constant along the symmetry axes of a rotating asymmetric top. The labels K_a (or K_{-1}) and K_c (or K_1) are used instead, which represent the projection of the total angular momentum onto the symmetry axis of the molecule in the prolate and oblate limiting cases, respectively.[18] Consequently, rotational

energy levels in asymmetric tops are denoted as J_{K_a,K_c}.

Additionally, the inertial defect (Δ), calculated as $\Delta = I_c - I_a - I_b$, provides a measure of a molecule's deviation from planarity. A perfectly planar and rigid molecule would have ($\Delta = 0$). To further quantify the degree of asymmetry within a molecule, a parameter known as Ray's asymmetry parameter (κ) is used. This parameter takes on values ranging from -1 indicating a perfectly symmetric prolate top through 0 representing the highest degree of asymmetry to +1 signifying a perfectly symmetric oblate top. The equation for (κ) is:

$$\kappa = \frac{2B - A - C}{A - C}. \tag{2.14}$$

A rotational transition arises from the interaction between the electric dipole moment and the electric field component of electromagnetic radiation. The selection rules governing the allowed transitions for asymmetric tops are summarized in Table 2.2. The transitions with ΔJ = -1 form a P-branch, $\Delta J = 0$ form a Q-branch, and ΔJ = +1 form an R-branch.[18]

Table 2.1
Selection rules for asymmetric top transitions (Dipole moment types).[18]

Dipole moment component	Transition type	ΔJ	ΔK_a	ΔK_c
μ_a	a-type	0,±1	0 (±2,..)	±1 (±3,..)
μ_b	b-type	0,±1	±1 (±3,..)	±1 (±3,..)
μ_c	c-type	0,±1	±1 (±3,..)	0 (±2,..)

The rigid rotor model neglects the flexibility of real molecules. During rotation, centrifugal forces cause slight distortions that lead to deviations between observed and rigid rotor-predicted transition frequencies. This effect becomes more pronounced in higher rotational states. To improve spectral modeling, centrifugal distortion constants are introduced. These quantify the extent of distortion in the molecule's rotational energy levels. Specific constants, like the commonly used D_J, D_{JK}, D_K, d_1 and d_2,[18] account for various aspects of distortion. Incorporating these constants refines calculated energy levels, improving the agreement between theoretical and observed spectra.

2.1.3 Vibrational spectroscopy

Vibrational spectroscopy, also known as infrared (IR) spectroscopy, is a method used to probe the vibrational modes of molecules. For a non-linear molecule with N atoms, there are a total of $3N$ degrees of freedom; this includes 3 translational, 3 rotational, and $3N - 6$ vibrational degrees of freedom. In the case of a linear molecule, which exhibits only 2 rotational motions, the normal modes of vibrational motion are slightly different,

amounting to $3N - 5$.[16]

The simplest quantum model used to describe molecular vibrations is the harmonic oscillator. It models the potential energy $E(r)$ of a chemical bond as a quadratic function of the displacement from its equilibrium bond length $r - r_e$:

$$E(r) = \frac{1}{2}k(r - r_e)^2, \tag{2.15}$$

where k is the force constant. The discrete energy levels of the vibrational states of the harmonic oscillator are evenly spaced and quantized as follows:

$$E_v = (v + \frac{1}{2})hf \tag{2.16}$$

where f is the frequency of oscillation, h is Planck's constant, and v is the vibrational quantum number ($v = 0, 1, 2, ...$).

However, real molecules exhibit anharmonic behavior, deviating from the ideal harmonic oscillator model. The Morse potential approximates this anharmonicity, accurately describing the potential energy of a chemical bond at both short and long interatomic distances. At distances shorter than the equilibrium bond length (r_e), the potential energy increases exponentially. For distances greater than r_e, it approaches the dissociation energy (D_e). The constant factor a in the Morse potential denotes bond stiffness.[16]

$$E(r) = D_e[1 - \exp(-a(r - r_e))]^2 \tag{2.17}$$

In the case of anharmonic oscillators, the vibrational energy levels are not evenly spaced and converge at higher energies.

Vibrational modes are visible in an IR spectrum if a change in the dipole moment occurs during the vibration. The selection rules governing the vibrational transitions in the case of harmonic oscillators are $\Delta v = \pm 1$, meaning only transitions between adjacent vibrational levels are allowed. However, in the case of anharmonic oscillators, the selection rules are more relaxed. In addition to the fundamental transitions ($\Delta v = \pm 1$), overtones ($\Delta v = \pm 2, \pm 3, ...$) and combination bands are also allowed, although with lower intensities.

2.2 | Spectroscopic techniques

This section details the principles and fundamentals of REMPI and LIF, two spectroscopic techniques employed in this thesis.

2.2.1 Resonance-enhanced multiphoton ionization (REMPI)

Resonance-enhanced multiphoton ionization[19–22] is a spectroscopic technique that selectively detects and analyzes molecules by exploiting their unique energy level transitions. It involves the excitation of molecules to higher energy states through the resonant absorption of multiple photons, followed by ionization through subsequent photon absorption. The resonant nature of the initial excitation step significantly enhances ionization efficiency and selectivity. Once ionized, the resulting ions are analyzed using a time-of-flight mass spectrometer (TOF-MS) based on their mass-to-charge ratio (m/z). This powerful combination enables detailed characterization of molecular species within a mixture, providing valuable insights into their structure.

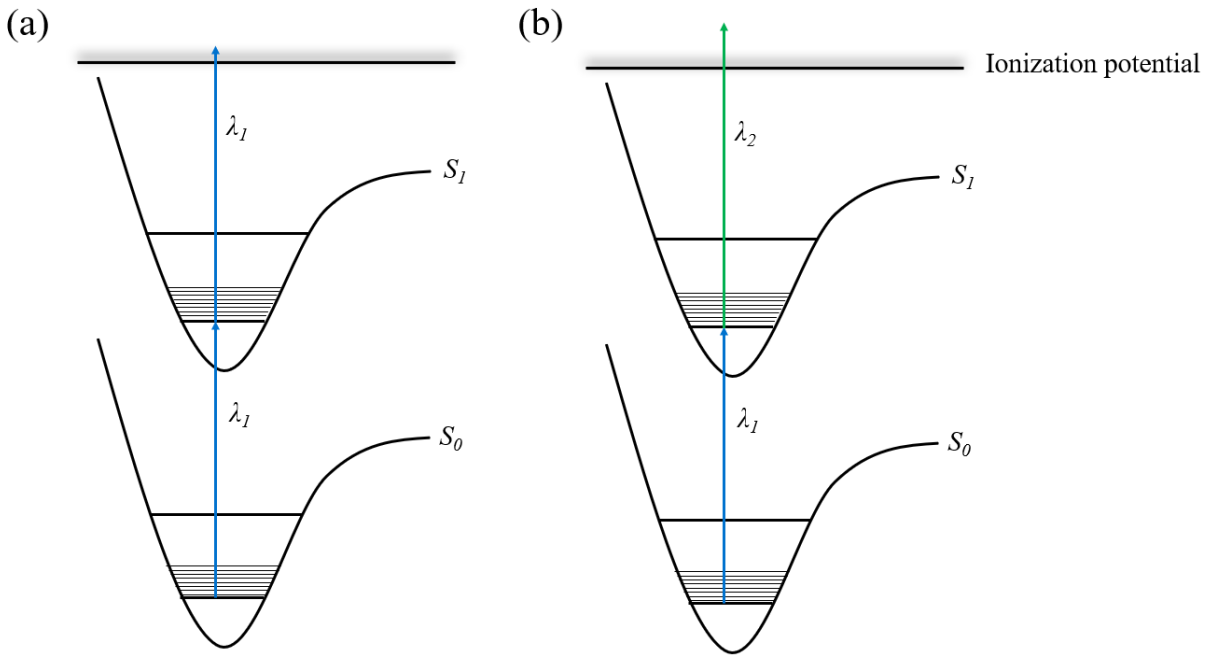

Fig. 2.2. Schematic representation of one-color (1+1) REMPI and two-color (1+1') REMPI schemes. In both processes, the molecule is promoted from the ground electronic state (S_0) to a resonant excited state (S_1) and subsequently ionized, forming a positively charged ion (M^+).

REMPI processes are typically described by the notation $n + n'$, representing the sequence of photon absorption events. Here, n photons excite the molecule to a resonant state, and n' photons subsequently ionize it. REMPI can be performed with a single laser wavelength (one-color scheme) or two different wavelengths (two-color scheme) for excitation and ionization. This thesis utilizes both processes, as illustrated in figure 2.2.

In this work, one-color (1+1) REMPI was employed to obtain a vibrationally resolved UV spectrum of the $S_1 \leftarrow S_0$ transition, enabling the identification of the origin band and several vibrational features through comparison with theoretical calculations. Additionally,

two-color (1+1') REMPI was utilized to determine the lifetime of the S_1 state. Details of these analyses are presented in Chapter 4.

2.2.2 Laser-induced fluorescence (LIF)

Laser-induced fluorescence is a versatile spectroscopic technique that reveals a molecule's electronic, vibrational, and rotational structure. A tunable laser precisely excites molecules from their ground electronic state (S_0) to a higher energy state (often S_1 or higher). Subsequent relaxation to lower energy states results in the emission of red-shifted fluorescence, which is then collected and measured by a photodetector (depicted in figure 2.3).

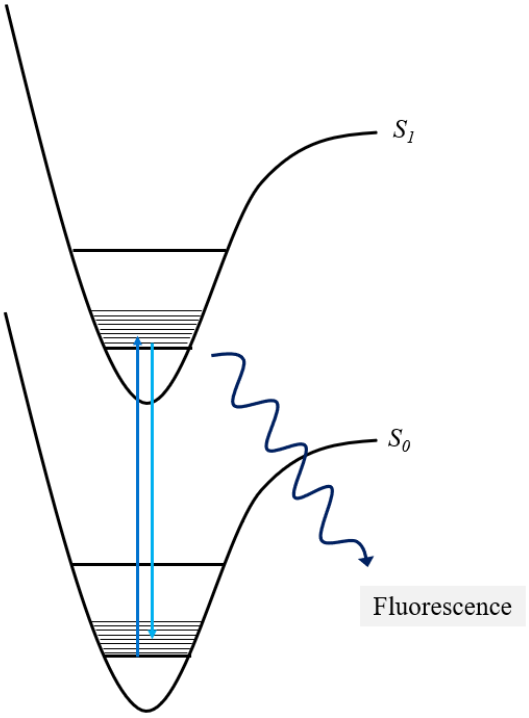

Fig. 2.3. Schematic illustrating the principles of LIF. A molecule absorbs a photon, transitioning to a higher electronic state (S_1). Subsequent relaxation to the ground state (S_0) results in the emission of a lower-energy fluorescence photon depicted here by a wavy arrow.

Scanning the excitation laser wavelength and monitoring the resulting fluorescence intensity yields an excitation spectrum, revealing detailed information about the molecule's energy levels. In this thesis, we measured the LIF excitation spectrum of 1-phenylethanol using a narrow linewidth laser to resolve the rotational transitions of the $S_1 \leftarrow S_0$ transition, providing insights into the molecule's excited-state rotational energy levels.

2.3 | Computational methods

This section provides a brief overview of DFT and TD-DFT, the foundational theories underpinning the electronic structure calculations performed with Gaussian software in

this study.

2.3.1 Density functional theory (DFT)

Density functional theory† is a computational method employing electron density, rather than wavefunctions, to investigate the electronic structure of materials.[24] The Hohenberg-Kohn theorem[25] establishes that a system's ground state properties are uniquely determined by its electron density. In DFT, the total energy is expressed as:

$$E_{\text{total}}[\rho] = T[\rho] + J[\rho] + E_{\text{xc}}[\rho] + E_{\text{ne}}[\rho] \tag{2.18}$$

where $T[\rho]$ is the kinetic energy, $J[\rho]$ the coulomb repulsion, $E_{\text{xc}}[\rho]$ the exchange-correlation energy, and $E_{\text{ne}}[\rho]$ the nucleus-electron interaction energy. The exchange-correlation term, $E_{\text{xc}}[\rho]$, is crucial, accounting for complex electron interactions not included in other terms.

DFT calculations utilize the Kohn-Sham equations[26], simplifying the problem to non-interacting electrons in an effective potential:

$$\hat{f}^{\text{KS}}\psi_i = \epsilon_i\psi_i, \tag{2.19}$$

where, $\hat{f}^{\text{KS}}$ is Kohn-Sham operator and is given as :

$$\hat{f}^{\text{KS}} = -\frac{1}{2}\nabla^2 + V_s(\mathbf{r}) \tag{2.20}$$

The effective potential $V_s(\mathbf{r})$ includes the exchange-correlation potential $V_{\text{xc}}(\mathbf{r})$, derived from the corresponding energy functional. DFT calculations iteratively adjust the electron density until convergence.

The choice of exchange-correlation functional significantly impacts accuracy. Common functionals include the local density approximation (LDA)[27] and the generalized gradient approximation (GGA)[28]. For systems with strong electron correlation, hybrid functionals like B3LYP[29] are preferred, combining Hartree-Fock exact exchange with density-functional exchange-correlation, improving accuracy in predicting chemical properties and reactions.

2.3.2 Time-dependent density functional theory (TD-DFT)

Time-dependent density functional theory[30] extends the principles of DFT to investigate the dynamic properties and excited states of quantum systems. TDDFT enables the exploration of phenomena such as electronic excitations and time-dependent processes,

†For a comprehensive introduction to DFT and the notation used in this section, please refer to Principles and Applications of Quantum Chemistry by V. P. Gupta[23]

which are inaccessible to conventional DFT. Central to TDDFT is the Runge-Gross theorem,[31] establishing a one-to-one correspondence between the time-dependent external potential and the electron density.

$$\Psi(t) = e^{-i\phi(t)}\Psi[\rho, \Psi_0](t) \tag{2.21}$$

Here, $\Psi(t)$ represents the time-dependent wave function, $\phi(t)$ is a time-dependent phase factor, and $\Psi[\rho, \Psi_0](t)$ is a functional determining the wavefunction at time t based on the electron density ρ and the initial state wave function Ψ_0. The electron density ρ evolves under the influence of a time-dependent external potential $V_{\text{ext}}(t)$:

$$V_{\text{ext}}(t) = \sum_{i=1}^{N} v_{\text{ext}}(\mathbf{r}_i, t) \tag{2.22}$$

where $v_{\text{ext}}(\mathbf{r}_i, t)$ is the external potential acting on electron i at position $\mathbf{r}_i$ and time t, and N is the total number of electrons.

TD-DFT calculations typically involve solving the time-dependent Kohn-Sham equations.[32] The linear-response approach simplifies the study of systems under small perturbations, facilitating the calculation of excitation energies and system responses to external fields. The key equation in linear-response TDDFT (LR-TDDFT) is the response function,[33] relating changes in electron density to perturbations in the external potential:

$$\rho_1(\mathbf{r}, t) = \int_0^\infty dt' \int d\mathbf{r}' \chi(\mathbf{r}t, \mathbf{r}'t')\delta v_{\text{ext}}(\mathbf{r}', t') \tag{2.23}$$

Here, $\rho_1(\mathbf{r}, t)$ is the first-order change in electron density at position $\mathbf{r}$ and time t, $\chi(\mathbf{r}t, \mathbf{r}'t')$ is the density-density response function, and $\delta v_{\text{ext}}(\mathbf{r}', t')$ represents a small time-dependent perturbation to the external potential at position $\mathbf{r}'$ and time t'.

Analysis of the density-density response function and its frequency components reveals the system's behavior under various conditions. TD-DFT thus extends DFT's capabilities to dynamic and excited-state phenomena, providing a comprehensive framework for studying systems under time-dependent conditions, particularly valuable for applications involving light-matter interactions and electronic excitation's.

CHAPTER 3

Methods

This chapter outlines the computational details employed in the investigation of the molecule's ground and first electronically excited state properties. Next, described is the experimental details of the setup utilized for performing both low- and high-resolution UV spectroscopy. Finally, presented is the spectral fitting procedure using the PGOPHER software for analysis of the rotationally resolved LIF spectrum.

3.1 | Computational details

I performed theoretical investigations of the molecule's ground and first excited electronic state properties using the DFT[34] and TD-DFT[30] methods. These calculations were implemented within the Gaussian 16 software[35]. We selected the B3LYP hybrid functional and the 6-311++G(d,p) basis set[29], with empirical dispersion correction. The results section provides a detailed justification for this choice. We used GaussView[36] to visualize optimized geometries, vibrational modes, and relevant calculated data.

3.2 | Experimental details

Figure 3.1 illustrates the experimental setup used for both low- and high-resolution UV spectroscopy. The setup employs an ultra-high vacuum system with two differentially pumped chambers: a source chamber and a detection chamber. This discussion begins with the source chamber, followed by the detection chamber, which incorporates setups for both REMPI-TOF and LIF spectroscopy.

3.2.1 Source chamber

A liquid sample of racemic 1-phenylethanol (obtained from TCI America with a purity of 98%) is introduced in a custom-designed sample holder located close to the front plate of a pulsed valve (General Valve, Series 9, nozzle diameter 0.9 mm). The sample holder and nozzle assembly are heated to a controlled temperature (~47° C) to facilitate vaporization of the liquid sample. The vaporized molecules are entrained in a carrier gas (helium or neon) and introduced into the source chamber through the pulsed valve. The backing pressure of the carrier gas is set to 3 bar. The pulsed valve operates at a repetition rate of

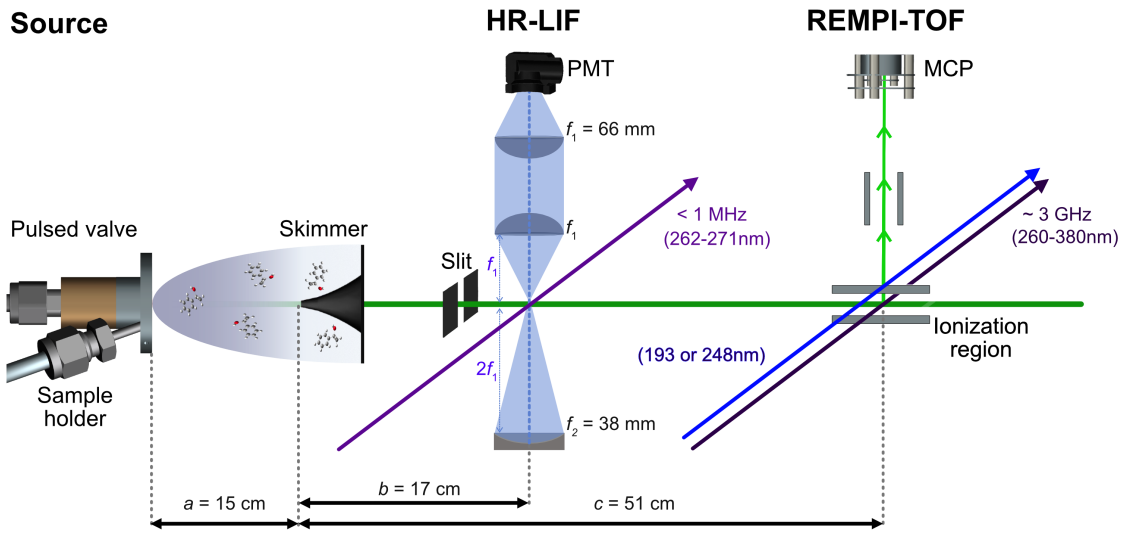

Fig. 3.1. Schematic diagram of the dual-chamber experimental setup for UV spectroscopy. Adapted with permission from ref.[37]. Liquid 1-phenylethanol molecules are introduced into the source chamber using a pulsed valve. Low-resolution UV spectra are acquired using REMPI-TOF mass spectrometry. High-resolution spectra are generated using a narrowband continuous-wave UV laser and the resulting fluorescence signal is detected by a PMT.

10 Hz for REMPI and 30 Hz for LIF measurements.

The pulsed valve initiates a supersonic expansion, and after traversing a skimmer (2 mm diameter, positioned ~0.15 m from the pulsed valve) a cold, collimated molecular beam is formed. This ensures a well-defined interaction region in the detection chamber. Separate pumping systems maintain low pressures in both chambers; typical source chamber pressures are $\sim 10^{-6}$ mbar for REMPI and $\sim 10^{-5}$ mbar for LIF during valve operation. The detection chamber maintains typical vacuum conditions of $\sim 10^{-7}$ mbar for both REMPI and LIF measurements.

3.2.2 REMPI-TOF setup

We acquire vibrationally resolved UV spectra using REMPI with TOF-MS. The experiment employs a frequency-doubled dye laser with the following specifications:

- Sirah PSCAN-D-18, UV resolution ~0.05 cm^{-1}.
- Tunable range: 260-380 nm.
- Pumped by a pulsed Nd-YAG laser at 355 nm, 250 mJ power.[37]
- Laser active medium: Coumarin 540A dissolved in ethanol (1.6 gL^{-1}).
- Frequency doubling is achieved using a potassium dihydrogen phosphate (KDP) crystal.

The setup also includes either a KrF (248 nm) or an ArF (193 nm) excimer laser for excitation. The pulsed nature of the dye laser necessitates synchronization with the

pulsed valve at a 10 Hz repetition rate. A wavemeter (HighFinesse WS6-600) is used to continuously monitor the dye laser output, ensuring precise wavelength measurement.

A TOF-MS detects the ions generated by the REMPI process. It is composed of repeller (VA_1) and extractor (VA_2) plates that provide the electric field required for ion acceleration. Prior optimization established a voltage difference (VA_1 = 1000 V, VA_2 = 756 V), ensuring efficient ion transmission. The accelerated ions travel through the flight tube towards a microchannel plate (MCP) detector positioned at the end. A potential difference (VD_1 = -1836 V) is applied to the MCP and then the signal is recorded using an oscilloscope*.

Precise timing control is crucial in REMPI experiments due to the inherently pulsed nature of the lasers involved. A Labview program controls the delays of the trigger pulses that are applied to the various components (source, lasers, and oscilloscope) to ensure optimal signal generation. Figure 3.2 provides a diagram illustrating this timing scheme. The results section offers a detailed discussion of the timing optimization process. Key timing parameters include:

- Δt_{dye}: Time difference between triggering the valve and the dye laser's Q-switch.
- $\Delta t_{excimer}$: Time difference between triggering the valve and the excimer laser.

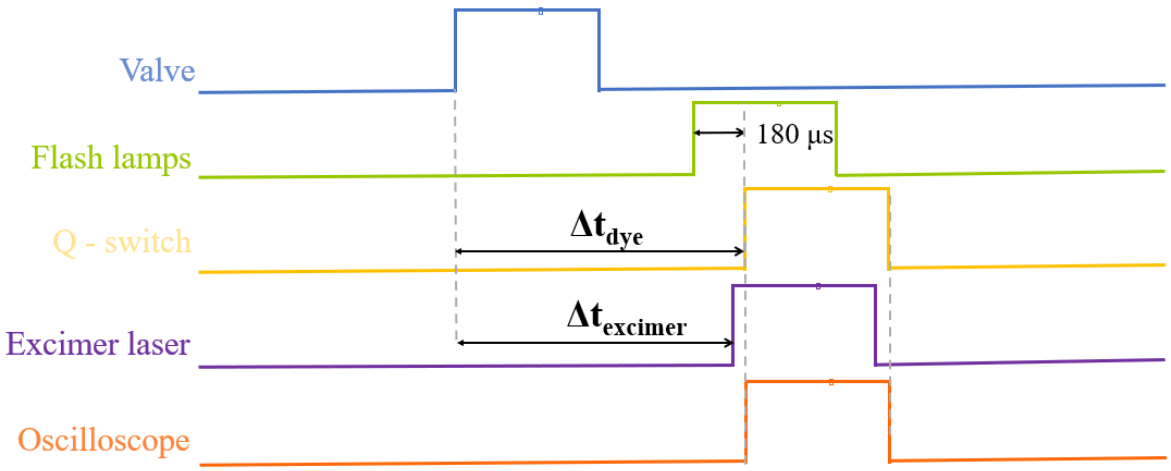

Fig. 3.2. Schematic of timing sequence for REMPI spectroscopy of 1-phenylethanol. The pulsed valve is triggered first. To optimize the interaction between the laser and the molecular beam, delay scans are performed by varying Δt_{dye}. For lifetime measurements, the delay between the dye laser (Δt_{dye}) and the excimer laser ($\Delta t_{excimer}$) is precisely controlled.

For one-color (1+1)-REMPI, we exclusively utilize a pulsed laser for both excitation and ionization. However, for two-color (1+1')-REMPI, we use a pulsed laser for excitation and an excimer laser for ionization. This thesis uses the two-color REMPI scheme to measure

*(National Instruments PXIe-5160)

the lifetime of the first electronically excited state, which is done by performing time delay scans by precisely controlling the timing between the dye and excimer laser pulses. We use custom MATLAB scripts for data analysis, employing techniques such as signal averaging, moving average filtering, and baseline correction. For further interpretation, we visualize and analyze the processed REMPI spectra in MATLAB.

3.2.3 LIF setup

We acquire the rotationally resolved high-resolution UV spectrum of 1-phenylethanol using LIF detection (figure 3.1). A continuous-wave, frequency-quadrupled high-power diode laser (TOPTICA, TA-FHG pro) is used as the excitation source. This laser offers the following key features:

- Tuning range: 262-271 nm
- Mode-hop-free tuning range: ~50 GHz
- Output power: above 50 mW
- Linewidth: < 1 MHz

A wavemeter (HighFinesse WS8-10) with an absolute accuracy of ~20 MHz in the UV region precisely measures the output wavelength of the frequency-doubled light. This precision allows for accurate determination of the transition frequencies.

Several measures are implemented to mitigate Doppler broadening of the spectral lines. A 2 mm wide slit, positioned 2.5 cm upstream of the laser interaction region, collimates the molecular beam. This collimation reduces the spread of interaction angles and minimizes Doppler broadening by reducing the transverse velocity spread. Careful perpendicular alignment of the laser with respect to the molecular beam avoids Doppler shifts. We achieve this by retro-reflecting the laser, ensuring that only the residual off-axis velocity distribution significantly affects the spectral linewidth. Combining these techniques resulted in a FWHM linewidth of approximately 54 MHz when using helium as a carrier gas.

For LIF signal collection, we employ a concave mirror and a combination of two plano-convex lenses (see figure 3.1). The fluorescence signal is collected perpendicularly to both the excitation laser and the molecular beam, which minimizes background scattering from the interaction region. To further reduce the recording of scattered excitation light, we use a high-reflectivity 266 nm laser mirror as an effective reflective filter. This mirror efficiently transmits off-resonance fluorescence at wavelengths greater than ~275 nm. The results section discusses the specific details regarding the optimal placement of this mirror for maximizing the signal-to-noise ratio.

A PMT (Hamamatsu R7154) detects the collected fluorescence light. The PMT's digitized output is recorded using an oscilloscope[†]. We use Labview for data acquisition and process and analyze the recorded data in MATLAB.

3.3 | PGOPHER fitting: Overview

The rotationally resolved LIF spectrum is analyzed by fitting it to simulations generated within the PGOPHER software package.[38] To generate the initial simulation, we provide PGOPHER with calculated rotational constants for the S_1 state and experimentally determined rotational constants for the S_0 state.[11] To understand the experimental spectrum, we need to assign transitions.

To initiate the assignment process, we utilize the combination difference technique, explained here with an example. We know that the frequency difference between 1_{11} and 1_{01} in the ground state is 2362 MHz .[11] There are 8 allowed, in general rotational transitions to the excited state, These transitions can be divided into 4 groups as shown in figure 3.3.

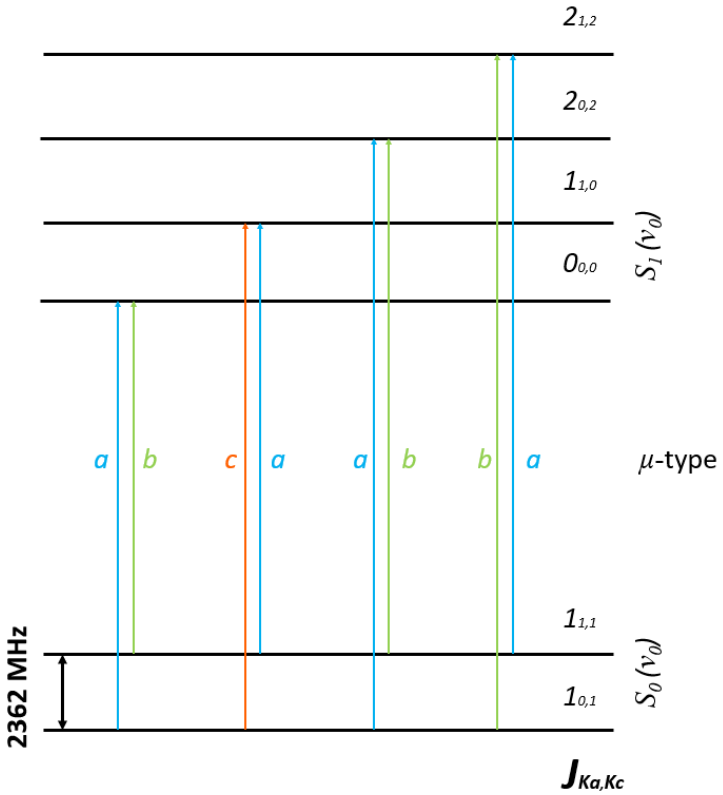

Fig. 3.3. The figure illustrates eight rotational transitions originating from the ground electronic state (labeled 1_{01} and 1_{11}) to the first excited electronic state. Each transition is assigned a label (a, b, or c), corresponding to the dipole moment type (μ_a, μ_b, or μ_c) involved in the transition.

[†]National instruments PXIe-5160

The frequency difference between the two transitions within each group is 2362 MHz. This difference allows to assign the quantum numbers of rotational levels in the ground state for each 8 transitions. Guided by selection rules and the expected frequency order, we then assign rotational quantum numbers in the excited electronic state. Importantly, each transition pair has differing dipole moment types, influencing the relative line intensities within each pair.

Based on the combination difference technique, we identify the eight transitions in the experimental spectrum and assign them. PGOPHER utilizes these assignments to fit the spectrum and generate a new simulation. Further transitions in the experimental spectrum are assigned by comparison with the simulated spectrum. This iterative process of assigning transitions and refining simulations continues until the final simulation accurately reproduces all observed transitions.

CHAPTER 4

Results and Discussion

This chapter is divided into three sections. The first section presents theoretical investigations of the molecule's ground and first electronically excited state properties. The second details the vibrationally resolved REMPI spectra, its analysis, and excited-state lifetime measurements. The final section presents the obtained high-resolution LIF spectrum and their interpretation.

4.1 | Theoretical Investigation

In this section, I present results and discuss theoretical investigations into the most stable conformer of 1-phenylethanol. A potential energy surface (PES) scan was used to identify this conformer, followed by geometrical optimization and the calculation of its spectroscopic parameters. Additionally, vibrational frequencies were determined for the ground and the first electronically excited states. Finally, the one-photon absorption spectrum, simulated using the Franck-Condon Herzberg-Teller (FCHT) approximation, is presented.

4.1.1 Computational modeling

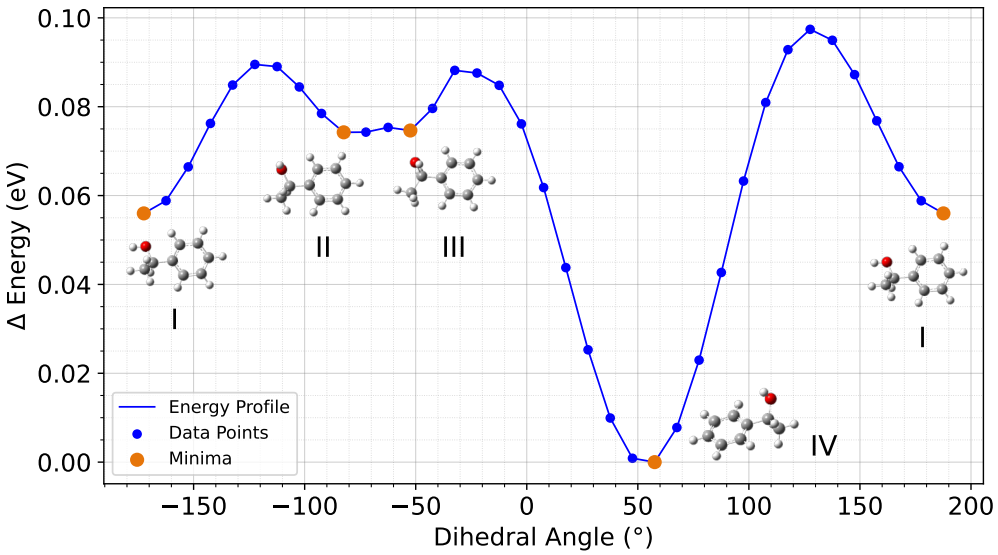

Fig. 4.1. PES of 1-phenylethanol, depicting energy variations as a function of the dihedral angle associated with OH group rotation.

Previous experimental observations in pulsed molecular jets using helium as a carrier gas revealed a single, predominant conformer[11,39] of 1-phenylethanol in the molecular beam that corresponds to its most stable form. Guided by this, we computationally investigated this specific conformer.

We began by generating a potential energy surface (shown in figure 4.1). The PES was constructed by varying the dihedral angle associated with OH group rotation in 10° increments. It reveals four minima (labeled I, II, III, and IV), each representing a distinct conformer with a unique OH orientation. Conformer IV exhibits the global minimum at a dihedral angle of approximately 55° ($\angle C_3C_{12}OH$), and was thus selected for further computational analysis.

4.1.2 Geometry optimization

Initial analysis focused on geometry optimization across various theoretical methods to determine which model could most accurately reproduce the experimentally observed ground state rotational constants.[11] This comparison was essential to select a reliable computational model, capable of accurately predicting molecular properties, for further investigations. A detailed comparison of these methods, presented in Table 4.1, reveals the B3LYP/6-311++G(d,p) method as the most suitable choice for computational modeling.

Table 4.1
Comparison of experimental and calculated rotational constants for 1-phenylethanol using various theoretical methods.

Method/Basis Set	*A* (MHz)	*B* (MHz)	*C* (MHz)
Experimental	3465	1103	981
B3LYP/aug-cc-pVTZ	3488	1097	981
B3LYP/6-311++G(d,p)	3471	1093	977
MP2/6-311++G(d,p)	3455	1099	984
WB97XD/6-311++G(d,p)	3487	1108	985
WB97XD/aug-cc-pVTZ	3503	1113	988

Figure 4.2 depicts the optimized geometry of the conformer, revealing a gauche conformation around the C_3-C_{12} bond. A notable feature is the intramolecular hydrogen bond between the OH group and the aromatic ring's π-electron system,[40] suggesting the importance of incorporating dispersion forces in the computational model. Grimme's D3 dispersion correction with Becke-Johnson damping (D3BJ)[41] was added to the B3LYP functional to address this.

This figure additionally displays the molecule's three inertial axes. The *a*-axis aligns with the phenyl ring plane, exhibiting the lowest moment of inertia. The *b*-axis lies perpendicular to this plane, while the *c*-axis is approximately perpendicular to both the

a and *b* axes. The methyl group (CH_3) occupies the opposite side of the phenyl ring relative to the OH group, potentially minimizing steric hindrance and contributing to the conformer's overall stability.

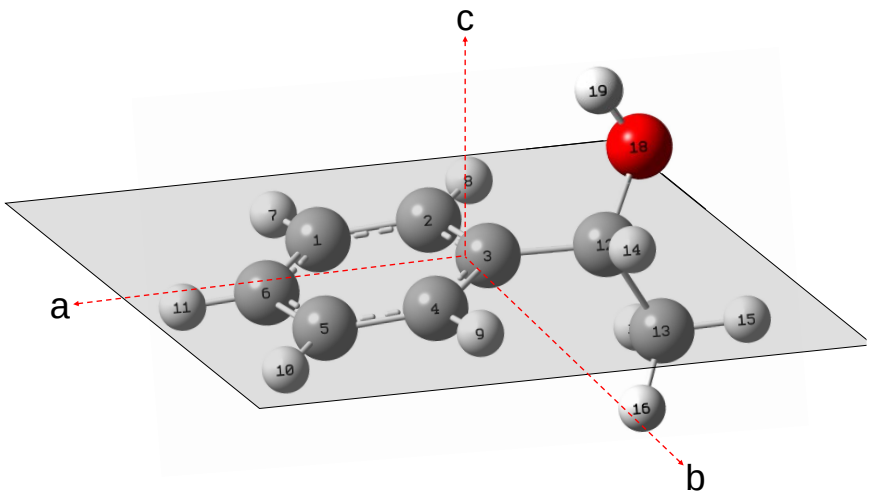

Fig. 4.2. Optimized geometry of 1-phenylethanol conformer IV: illustrating the three inertial axes.

4.1.3 Frequency analysis

The frequency analysis was performed for both the ground state and the first electronically excited state using an anharmonic approximation. This analysis yielded spectroscopic parameters, summarized in Table 4.2.

Table 4.2
Calculated spectroscopic parameters of 1-phenylethanol: rotational constants (*A*,*B*,*C*), quadratic centrifugal distortion constants, asymmetry parameter (κ) for ground and first electronically excited states, and transition dipole moments (μ_a, μ_b, μ_c) for the first excited state relative to the ground state.

Parameter	Ground state	Excited state
A (MHz)	3471.98	3367.08
B (MHz)	1099.67	1097.97
C (MHz)	982.48	964.51
μ_a	-	0.05
μ_b	-	-0.08
μ_c	-	-0.007
D_J (kHz)	0.103	0.089
D_K (kHz)	0.062	0.077
D_{JK} (kHz)	0.219	0.272
d_J (kHz)	-0.01	-0.011
d_k (kHz)	0.011	0.003
κ	-0.905	-0.889

These parameters include rotational constants (A, B, C), quadratic centrifugal distortion constants, the asymmetry parameter (κ) for both states, and the electronic transition

dipole moments for the first excited state relative to the ground state.

The observed decrease in rotational constants ($\Delta A = -104.9$ MHz, $\Delta B = -1.7$ MHz and $\Delta C = -17.97$ MHz) upon electronic excitation suggests a slight expansion of the molecular dimensions, primarily along the a and c axes. This indicates potential structural relaxation during the transition to the excited state. The minimal change in the asymmetry parameter κ suggests only minor alterations in molecular asymmetry upon excitation. These excited state rotational constants serve as initial parameters for spectral fitting of the experimentally measured spectrum using PGOPHER, facilitating initial simulation.

Additionally, this analysis yielded vibrational frequencies* for corresponding modes in both the ground and first electronically excited states, presented in Table 4.3.

Table 4.3
Calculated vibrational frequencies for the ground and first electronically excited states using anharmonic approximation.

Modes	Ground state $\widetilde{\nu}$ (cm^{-1})	Excited state $\widetilde{\nu}$ (cm^{-1})
Φ-R torsion	42	52
Φ-R deformation	127	93
CH_3 torsion	207	200
Φ-R deformation	252	222
Ring CC deformation	307	240
Ring bend	329	246
CH_3 bend	362	312
H-C-O-C-H torsion	413	344
Ring bend	485	353
C-C-O bending	549	463
Ring CC bend	618	518
Ring torsion	635	540
Ring torsion	714	573
Ring torsion	774	592
Ring torsion	780	598

4.1.4 Calculated spectrum

The one-photon absorption spectrum was simulated using the Adiabatic Hessian model[42], which provides information about the molecule's potential energy surfaces. Two approximations were employed: FC and the FCHT , which incorporate both the FC approximation and the dependence of the electronic transition dipole moment on nuclear coordinates. The FC approximation failed to reproduce vibrational bands in the 400-600 cm^{-1} region above the origin band, a feature accurately captured by the FCHT approximation. This

*The terms 'wavenumber' and 'frequency' are used interchangeably in this thesis, although the calculated values are expressed in cm^{-1}

discrepancy highlights the importance of incorporating vibronic coupling effects via FCHT for accurate spectral simulation.

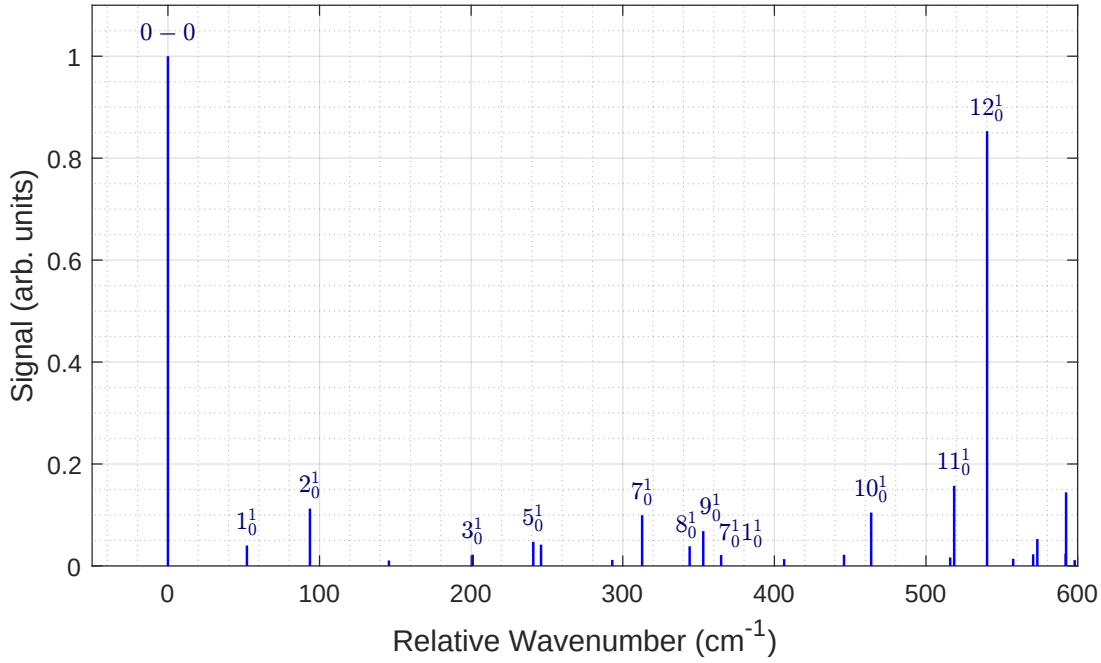

Fig. 4.3. Theoretical one-photon absorption spectrum of 1-phenylethanol: Normalized intensity versus relative wavenumber (cm^{-1}; referenced to the calculated origin band $0-0$ at 40139 cm^{-1}).

The simulated one-photon absorption spectrum, presented in figure 4.3, displays transitions with intensities exceeding 0.01. Transitions with intensities above 0.025 are distinctly labeled (blue lines) using the notation vibrational mode$_{\nu}^{\nu'}$, where ν and ν' represent the vibrational quantum numbers in the ground and first electronically excited states, respectively.

The spectrum is plotted in relative wavenumbers, with x-axis values given relative to the origin band at 40139 cm^{-1}. The calculated spectrum is characterized by a dominant $0-0$ band, a region of weak bands (250-350 cm^{-1}), and a cluster of bands centered around a peak at 450-550 cm^{-1} over the origin band.

This theoretical spectrum serves as a reference for understanding vibrational transitions in the experimentally obtained REMPI spectrum. By comparing and assigning observed peaks to their theoretical counterparts, we gain insight into the specific vibrational transitions of 1-phenylethanol upon electronic excitation. This comparison also allows us to assess the suitability of the chosen theoretical model for accurately representing the experimental observations.

The theoretical investigations performed in this section provides a foundation for interpreting the experimental results presented in the following sections.

4.2 | REMPI

This section presents results from REMPI experiments on 1-phenylethanol, detailing the identification of the REMPI signal, followed by investigating the influence of helium and neon carrier gases on the spectra. The experimental REMPI spectrum is compared to the theoretical absorption spectrum for vibrational feature assignment. Additionally, the rotational band contour scanned over the origin (0-0) band is analyzed. Finally, the excited state lifetime of the S_1 state is discussed.

4.2.1 Signal identification

To identify the 1-phenylethanol signal, the experimental setup, previously optimized for styrene oxide in prior studies, was adapted to generate a cold molecular beam (using styrene oxide as a reference).

An off-resonant ArF excimer laser, aligned perpendicularly to the molecular beam, was used for ionization within the TOF-MS. The resulting ion signal was collected by a MCP in a time-resolved manner.

TOF data (signal intensity vs. time) was collected and subsequently mass/charge-calibrated using two known timings:

1. $\boldsymbol{t_0}$: The laser-molecule interaction time, effectively equivalent to ionization time, is identified by a characteristic noise signal on the oscilloscope attributed to the excimer laser.

2. $\boldsymbol{t_{120}}$: The arrival time of styrene oxide, determined from previous experiments.

Mass calibration was achieved using the equation:

$$m/z = \frac{(t - t_0)^2}{k}, \tag{4.1}$$

This equation converts time-axis data to m/z values. The calibration constant k, required for this conversion, was determined from the flight time (t_{120}) of ions at $m/z = 120$ (styrene oxide) using:

$$k = \frac{(t_{120} - t_0)^2}{120}, \tag{4.2}$$

Figure 4.4 presents a representative mass spectrum obtained with ArF excimer laser ionization. The peak at m/z=122 corresponds to the molecular ion of 1-phenylethanol ($C_8H_{10}O^+$). The peak at $m/z = 107$, resulting from the loss of a CH_3 group from the

molecular ion, is likely the hydroxybenzyl cation ($C_7H_7O^+$), as shown in the following reaction:[43]

$$[C_8H_{10}O]^+ \rightarrow [C_7H_7O]^+ + CH_3, \tag{4.3}$$

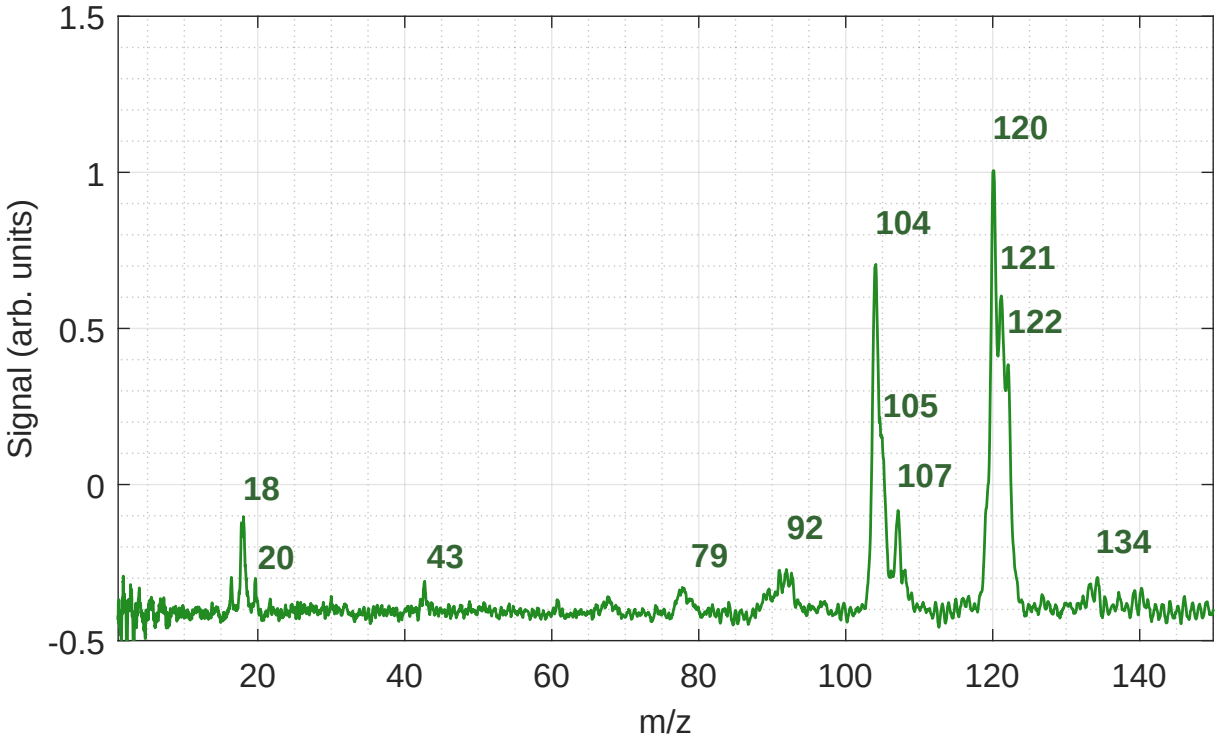

Fig. 4.4. Mass spectrum with key ion peaks labeled, obtained via excimer laser ionization.

However, this assignment is not unambiguous, as the hydroxytropylium cation presents an alternative structural isomer with the same mass.[43] The peak observed at (m/z = 105) likely corresponds to the benzoyl cation ($C_7H_5O^+$), formed via H_2 loss from the hydroxybenzyl cation.[43]

$$[C_7H_7O]^+ \rightarrow [C_7H_5O]^+ + H_2, \tag{4.4}$$

Additional peaks in the mass spectrum are likely attributable to:

- m/z = **43:** Acetyl cation.
- m/z = **92:** Toluene.
- m/z = **121:** ^{13}C isotopologue of styrene oxide.
- m/z = **134:** Residual indanol from previous styrene oxide experiments.
- m/z = **104:** Loss of water from the molecular ion of 1-phenylethanol.
- m/z = **18:** Water.

- $m/z = \mathbf{20}$**:** Neon.

Confirmation of 1-phenylethanol's presence in the molecular beam, and determination of its expected signal location on the time axis, allowed for targeted scanning with the pulsed dye laser to search for a REMPI signal. A scan from 36700 cm^{-1} to 37800 cm^{-1} in 0.7 cm^{-1} increments revealed an initial signal at approximately 37612 cm^{-1} (presented in figure 4.5).

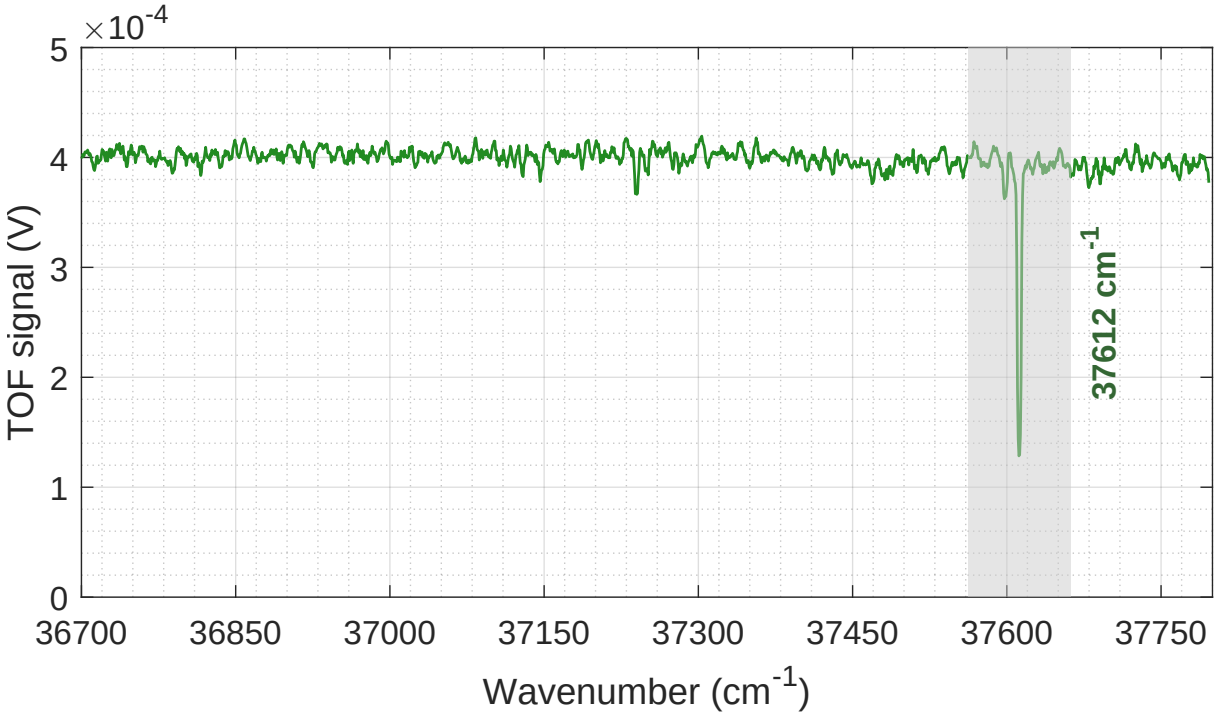

Fig. 4.5. Frequency scan of 1-phenylethanol using a dye laser. The resonance peak at approximately 37612 cm^{-1} indicates the molecule's ionization signal.

4.2.2 Influence of different carrier gases

To assess the influence of carrier gas choice on the cooling of the molecular beam and REMPI spectra, REMPI experiments were conducted using both helium and neon. The optimal experimental conditions for each gas were first established through time delay scans.

Delay scan

To obtain optimal signal-to-noise ratios and ensure cold molecular beams with both helium and neon carrier gases, we varied the time delay (Δt_{dye}) between the pulsed valve and dye laser operation. Due to differences in molecular speeds, the delay scan ranges for helium and neon differed (see figure 4.6). Optimal delays of approximately 550 μs for helium and 930 μs for neon were determined, aligning with their calculated molecular speeds (1800 m/s for helium, 800 m/s for neon).

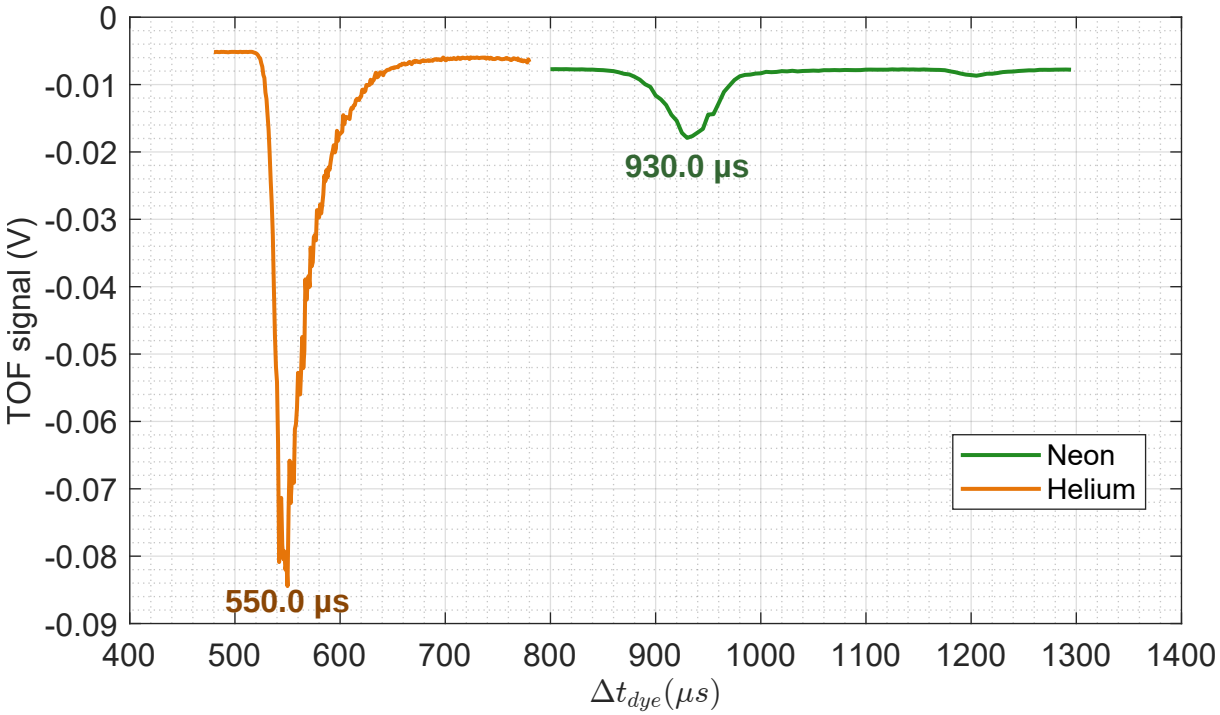

Fig. 4.6. Delay scan for helium and neon carrier gases. The graph illustrates how signal intensity varies with the delay time (Δt_{dye}) between the pulsed valve trigger and the pulsed dye laser Q-switch.

During these scans, notable differences emerged between the carrier gases. A small, additional peak appeared at later delay times in the neon data, likely due to a minor source imperfection. This peak was absent in the helium data, primarily due to the narrower delay range scanned. Additionally, helium yielded a tenfold higher signal intensity and a narrower spectral linewidth (FWHM of 28.5 μs compared to 50 μs for neon). These disparities likely arise from neon's longer flight time, potentially causing greater dispersion and a broader energy distribution in the molecular beam.

REMPI spectra

With the optimal time delays established, we investigated the influence of carrier gas choice on the (1+1) REMPI spectra of 1-phenylethanol. Spectra were recorded using both helium and neon, scanning a wavenumber range from 37500 cm^{-1} to 38200 cm^{-1} in 0.7 cm^{-1} intervals. Figure 4.7 presents the results, with helium data in orange and neon data in green. For clarity of comparison, the spectra are normalized to their respective maximum intensities.

Analysis of the spectra reveals similar peak profiles for both helium and neon carrier gases, suggesting comparable internal energy distributions within their respective molecular beams. This similarity indicates a lack of detectable gas-dependent conformational differences within the 1-phenylethanol molecular beam, aligning with literature supporting the predominance of a single conformer.[44] Due to comparable spectral cooling achieved with

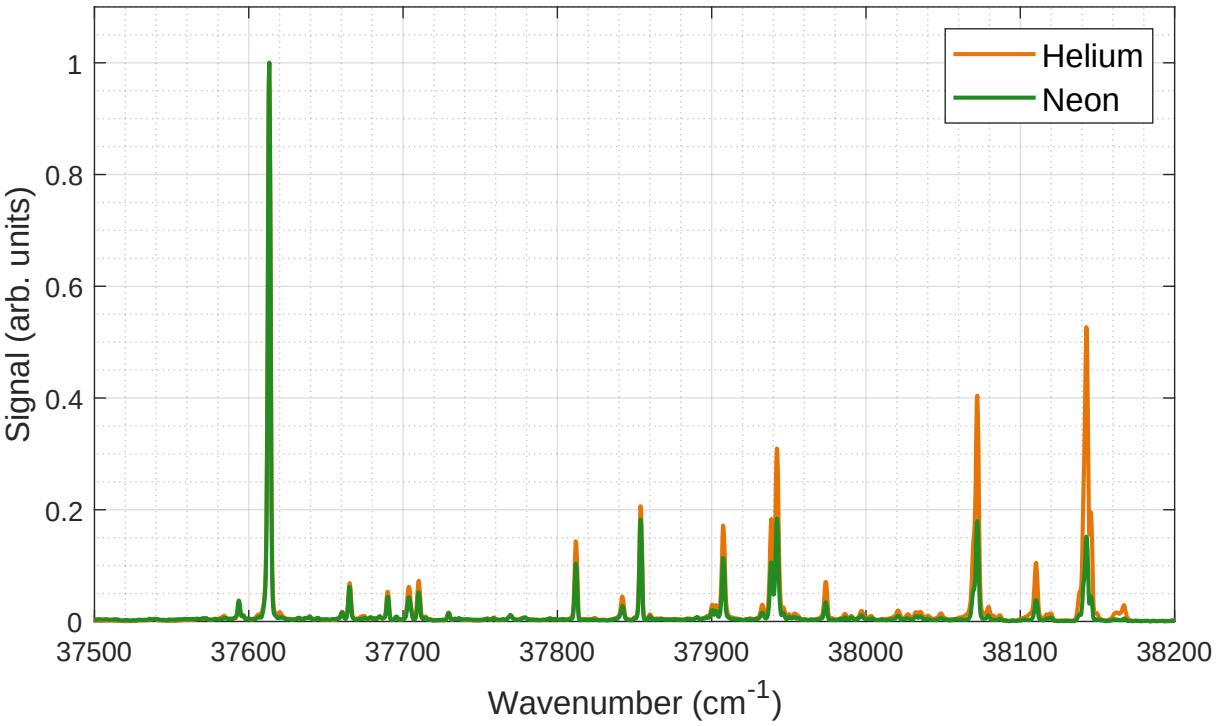

Fig. 4.7. Comparison of (1+1) REMPI spectra for 1-phenylethanol using helium and neon carrier gases. Intensities are normalized for comparison. (Note: Helium yields tenfold higher signal intensity prior to normalization.)

both gases, we selected helium as the carrier gas for subsequent spectroscopic investigations, owing to its nearly tenfold greater signal intensity compared to neon, as illustrated in figure 4.6.

4.2.3 Analysis of the REMPI spectrum

Comparison of the experimental and theoretical (Section 4.1.4) spectrum enabled assignment of the most intense experimental band at 37612 cm^{-1} as the origin transition, consistent with previous findings[45]. To facilitate further analysis, the experimental spectrum was offset by the origin band frequency (37612 cm^{-1}), while the theoretical spectrum was offset by its predicted origin at 40139 cm^{-1} (figure 4.8). All subsequent vibrational mode assignments reference these respective origins.

Analysis of the spectrum from left to right reveals peaks at -19 cm^{-1}, 52.5 cm^{-1}, 77 cm^{-1}, and 91 cm^{-1}, assigned to the 1-phenylethanol-water complex.[40] This is evident in the zoomed-in region of Figure 4.9, displaying the relative wavenumber range from -50 to 100 cm^{-1}.

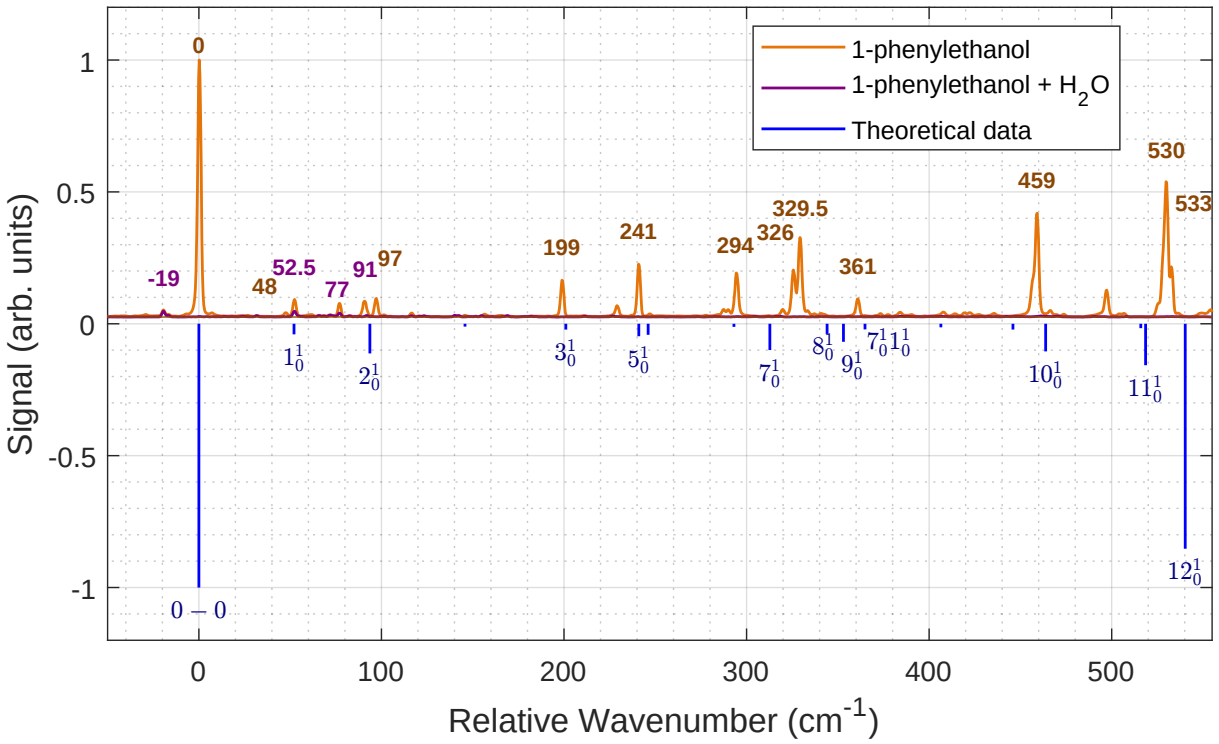

Fig. 4.8. Vibrationally resolved REMPI spectra of 1-phenylethanol and its water complex. The experimental spectrum (orange) is offset by 37612 cm^{-1} to align the origin band with the theoretical spectrum (blue), offset by 40139 cm^{-1}.

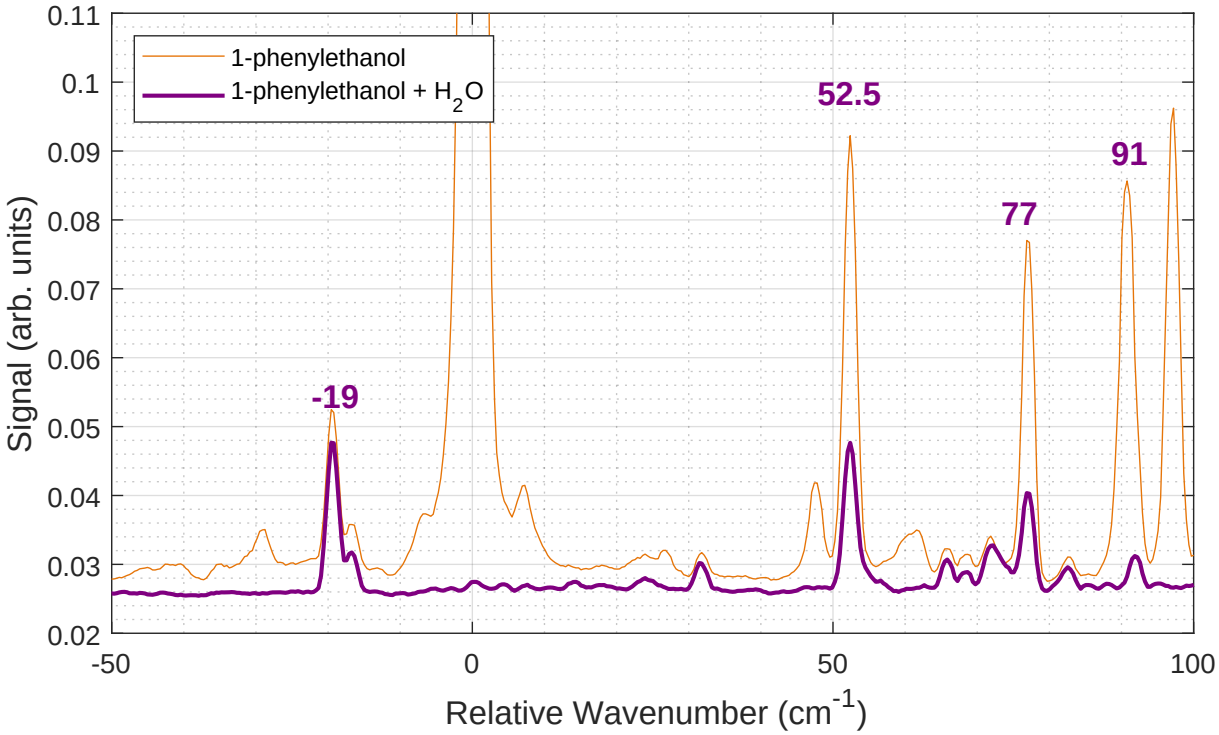

Fig. 4.9. Enlarged view of figure 4.8, emphasizing the low wavenumber region with respect to the origin band . Key vibrational mode transitions at -19, 52.5, 77, and 91 cm^{-1}, corresponding to the 1-phenylethanol-H_2O complex, are highlighted to facilitate their assignment in the experimental spectrum

The experimental peak at 48 cm^{-1} can be assigned to the theoretically predicted 1_0^1 transition, representing the fundamental transition of vibrational mode 1. This mode corresponds to the **Φ**-R torsion , which involves twisting of the phenyl ring relative to the rest of the molecule, inducing motion in the bonded ethanol group.

The peak observed at 97 cm^{-1} aligns with the theoretically predicted 2_0^1 transition, exhibiting a blue shift from its calculated position of 93.67 cm^{-1}. This peak corresponds to the fundamental transition of vibrational mode 2, characterized by a deformation of the dihedral angle between the phenyl ring and the ethyl group **Φ** deformation. The visualizations for the assigned vibrational modes are presented in the figure 4.10

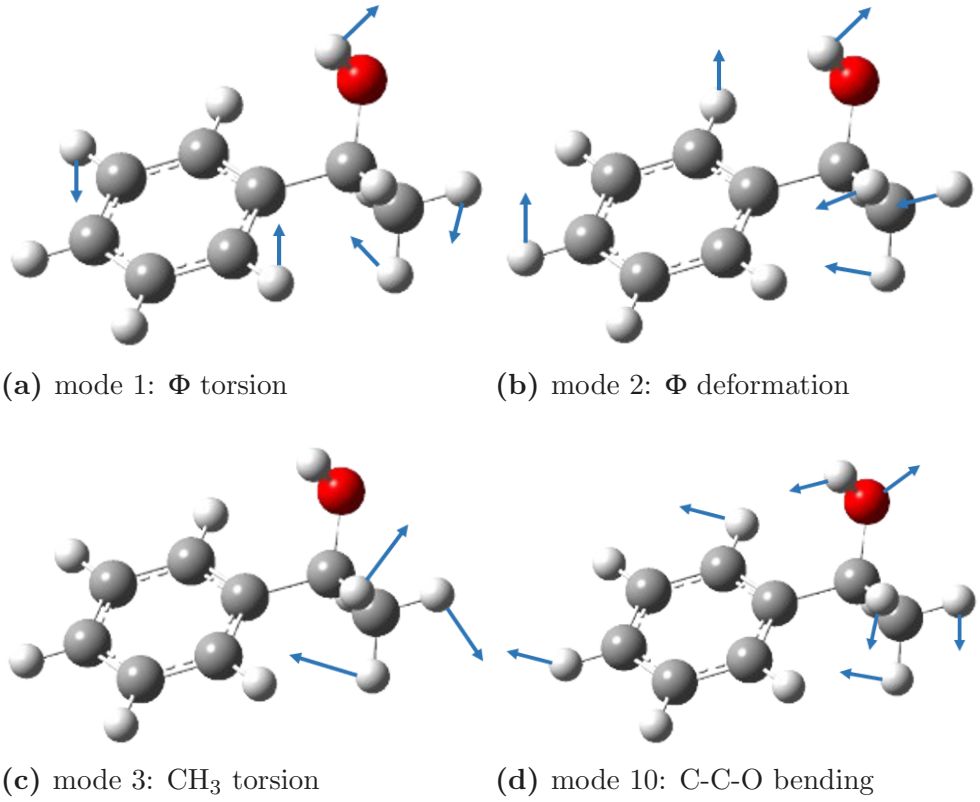

(a) mode 1: **Φ** torsion **(b)** mode 2: **Φ** deformation

(c) mode 3: CH_3 torsion **(d)** mode 10: C-C-O bending

Fig. 4.10. Depiction of assigned vibrational modes of the molecule. The images illustrate the directional motions associated with (a) mode 1: **Φ** torsion, (b) mode 2: **Φ** deformation, (c) mode 3: CH_3 torsion, and (d) mode 10: C-C-O bending.

The peak observed at 199 cm^{-1} is attributed to the theoretically predicted 3_0^1 transition, exhibiting a red-shift from its calculated position of 200.99 cm^{-1}. This peak corresponds to the torsional vibration of the CH_3 group within the -CH_2OH moiety of 1-phenylethanol.

The observed peak at 241 cm^{-1} lies in close proximity to both the theoretically predicted 5_0^1 (240 cm^{-1}) and 6_0^1 transitions, making a definitive assignment challenging.

In the 250-400 cm^{-1} region above the orgin band, significant discrepancies in both intensity and position between experimental and theoretical peaks preclude confident assignment of

vibrational modes based on the theoretical spectrum alone.

The peak at 459 cm^{-1} is tentatively assigned to the 10_0^1 fundamental transition, predicted at 463.83 cm^{-1}, corresponding to vibrational mode 10. This mode primarily involves C-C-O bending within the molecule, with a significant contribution from CH_3 bending. The peaks observed at 530 cm^{-1} and 533 cm^{-1} align with the 11_0^1 and 12_0^1 transitions, respectively, but assignment is difficult due to observed discrepancies in their intensities.

While theoretical calculations aid in assigning some experimental peaks, the inability to explain all observed features highlights the need for improved theoretical models and suggests that absorption band data alone may not be sufficient for a complete spectral understanding. Incorporating electronic circular dichroism (ECD) data may offer a valuable tool for assigning transition bands and enhancing the correlation between theoretical predictions and experimental results[46].

4.2.4 Rotational band contour

Following identification of the origin band in the REMPI spectrum, a scan with a resolution of 0.01 cm^{-1} was performed over this band. The resulting rotational band contour (RBC), presented in figure 4.11, features prominent P, Q, and R branches, providing initial insight into the rotational characteristics of the transition.

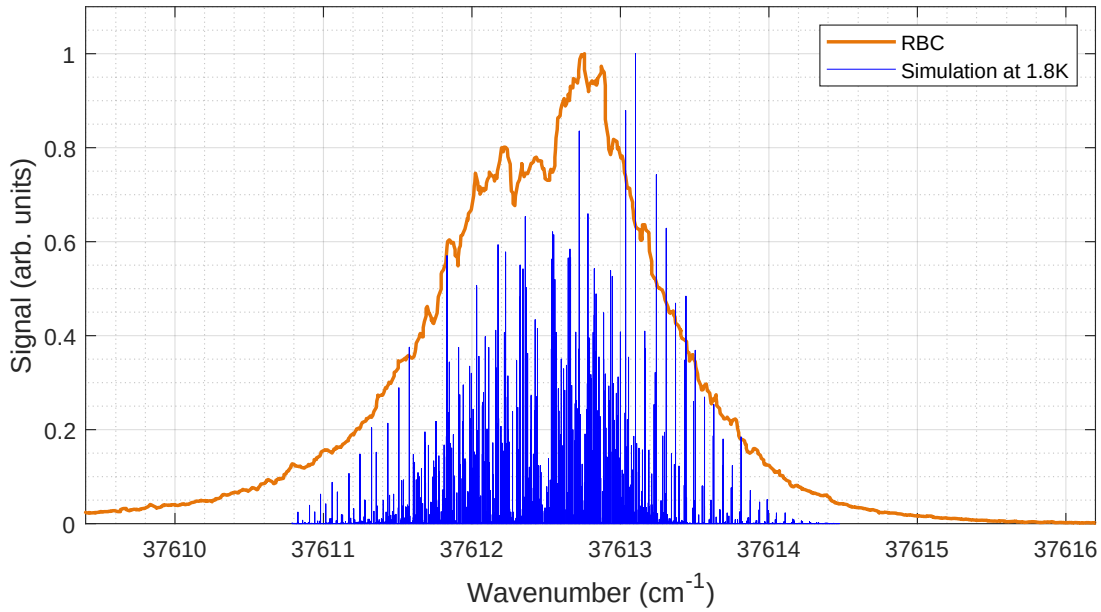

Fig. 4.11. Rotational band contour of 1-phenylethanol scanned over the origin band, compared with a PGOPHER simulation at 1.8 K.

A comparison of the observed rotational band contour with PGOPHER simulations of the rotationally resolved electronic spectrum for $S_1 \leftarrow S_0$ suggests a molecular beam temperature of approximately 1.8 K during REMPI measurements. While this provides

initial insight, a detailed rotationally resolved electronic spectrum recorded using LIF is presented in Section 4.3.3.

4.2.5 Lifetime measurements

Two pulsed laser systems, comprising a KrF excimer laser (248 nm) and a dye laser tuned to the $S_1 \leftarrow S_0$ transition (265.8 nm), were used to measure the S_1 excited state lifetime of 1-phenylethanol's most stable conformer. Both laser pulse energies were attenuated to prevent ion signal from one-color (1+1) REMPI processes and direct ionization.

Delay scans were acquired by varying the timing between the two laser pulses. The dye laser pulse selectively excites molecules to the S_1 state, and the subsequent excimer laser pulse ionizes those remaining in the excited state after a controlled delay. The resulting signal decay with increasing delay allows direct measurement of the excited state lifetime.

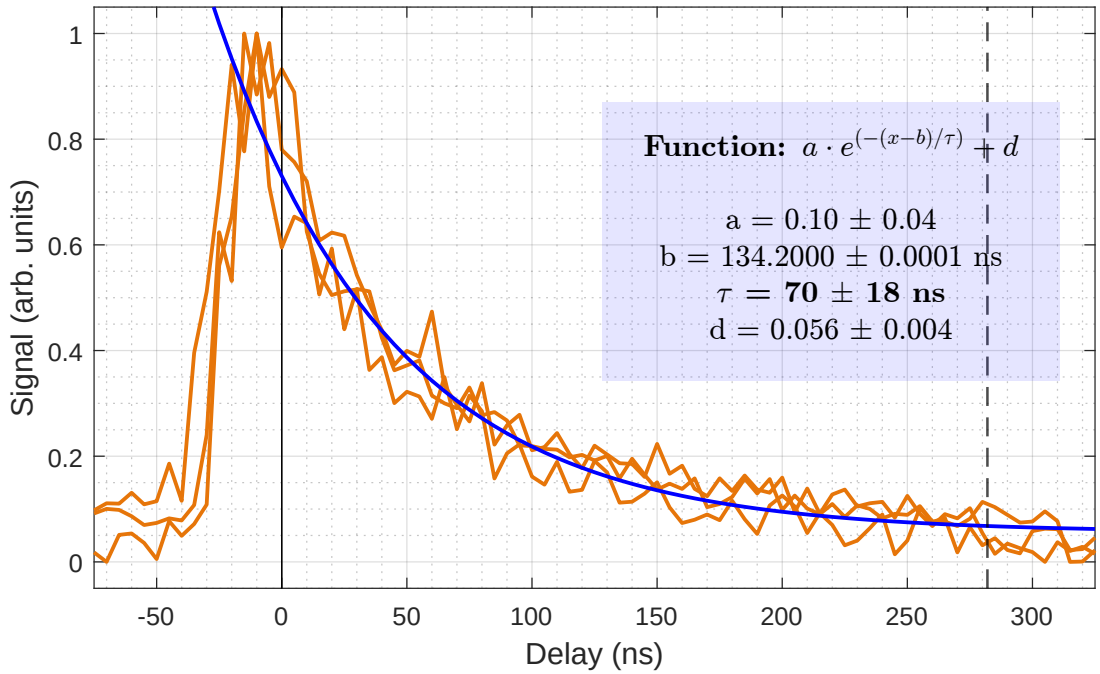

Fig. 4.12. Excited state lifetime measurements for 1-phenylethanol (S_1) using a two-color REMPI scheme. Orange plots represent three normalized experimental measurements (signal intensity vs. delay time in ns). The blue curve is a single exponential fit to the averaged data, following the model $a \cdot e^{-(x-b)/\tau} + d$. The inset table summarizes fit parameters a, b (ns), τ (ns), and d.

Delay scan measurements were fitted to a single exponential decay model, $(a \cdot e^{-(x-b)/\tau} + d)$, where a represents initial signal intensity, b a temporal shift, (τ) the measured lifetime, and d a baseline offset (figure 4.12). Fitting with a MATLAB script yielded a lifetime of 70 ± 18 ns (95% confidence limit).

Applying the Heisenberg uncertainty principle to this lifetime estimates a spectral broadening of approximately 2.2 MHz ($\Delta\nu = \frac{1}{2\pi\tau}$). This natural linewidth confirms the feasibility of employing high-resolution LIF with a narrow linewidth laser to resolve individual rotational transitions.

4.3 | LIF

This section presents results from LIF spectroscopy experiments on 1-phenylethanol. Initial efforts focused on mitigating scattered laser light and electronic noise to improve the signal-to-noise ratio. A high-resolution LIF spectrum recorded over the origin band, previously identified by REMPI, is presented. Analysis of the experimental spectrum through spectral fitting with a simulated spectrum yields rotational constants, providing insights into the first electronically excited state (S_1) rotational energy level structure and molecular geometry of 1-phenylethanol. These results and their implications are discussed in detail.

4.3.1 Evaluation of low-pass filters

The acquired LIF signal contained high-frequency components unrelated to the expected molecular signal. To potentially mitigate this noise, a frequency analysis was performed by inserting low-pass filters with varying cut-off frequencies (2.5 MHz, 5 MHz, 10.7 MHz, 25 MHz, and 50 MHz) between the PMT and the oscilloscope.

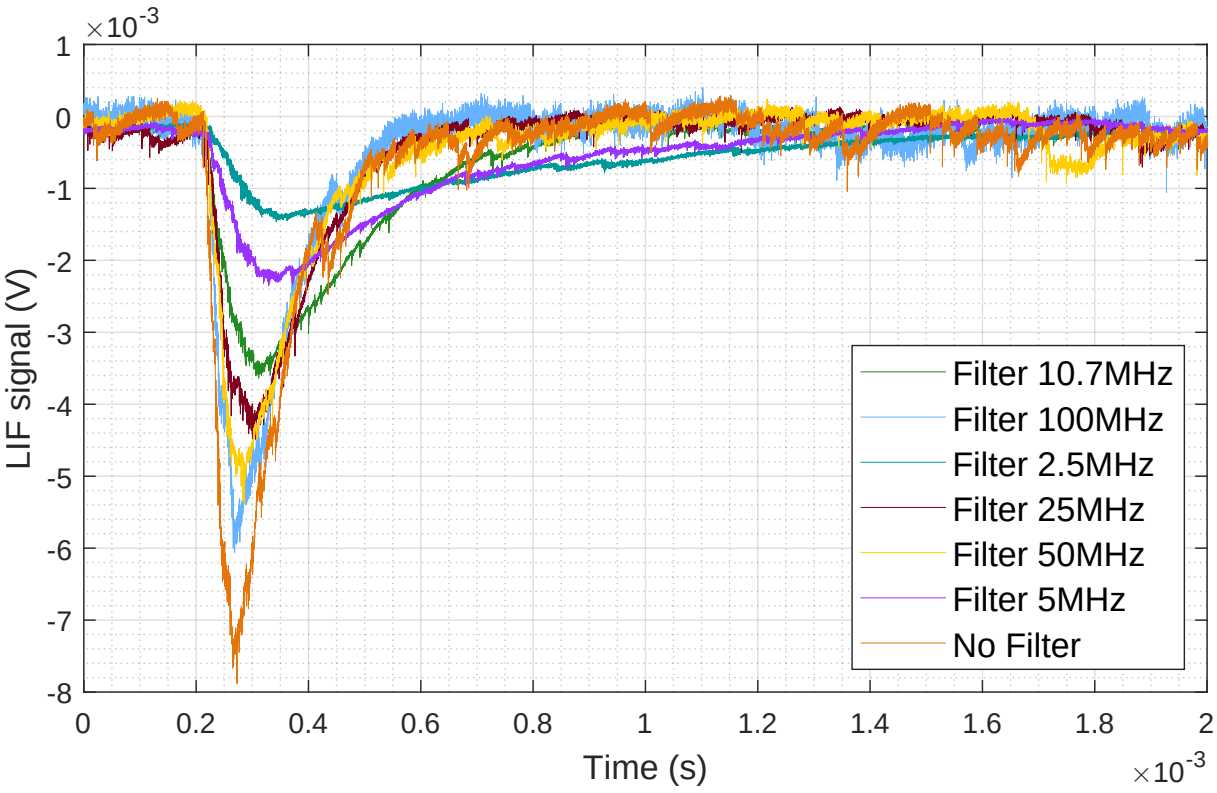

Fig. 4.13. The plot illustrates the LIF signal, showcasing the effects of various low-pass filters with cutoff frequencies of 2.5 MHz, 5 MHz, 10.7 MHz, 25 MHz, and 50 MHz, as well as a signal with no filter applied.

While numerous experimental factors can affect the frequency sensitivity of data acquisition, this investigation focuses solely on the impact of low-pass filtering, excluding other factors such as the oscilloscope's sampling rate.

The application of low-pass filters (as seen in figure 4.13) failed to attenuate the high-frequency noise present in the LIF signal, demonstrating the limitations of filtering in this scenario. As none of the tested filters effectively removed the noise, their use would have compromised signal intensity without providing substantial benefit. Consequently, the unfiltered signal was utilized for high-resolution LIF measurements.

While low-pass filtering proved ineffective, the presence of high-frequency noise necessitates further investigation into alternative noise-reduction strategies. Besides identifying and eliminating or shielding the actual noise sources, post-acquisition application of digital filtering techniques may offer greater control and precision in selectively targeting and eliminating these noise components while minimizing signal loss.

4.3.2 Mirror optimization for scattered light reduction

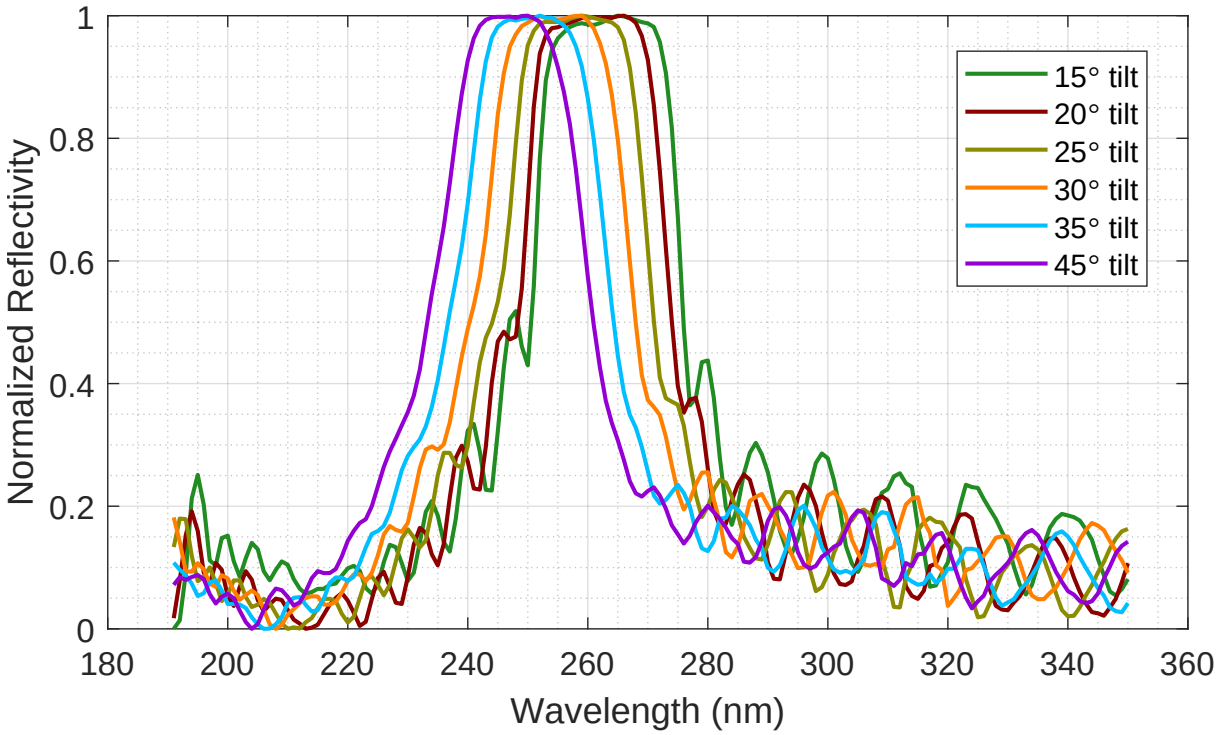

Fig. 4.14. Reflectivity range dependence on tilt angle (for high-reflectivity 266 nm mirror): This graph illustrates how the mirror's reflectivity range varies as a function of tilt angle, ranging from 15° to 45°.

The fluorescence signal was collected perpendicular to both the excitation laser and the molecular beam to minimize background scattering. A high-reflectivity 266 nm laser mirror was employed as a reflective filter before the PMT detector to further reduce scattered excitation light. To optimize the signal-to-noise ratio, we investigated the effect of mirror tilt angle on filtering effectiveness.

A commercial spectrometer (SPECORD 40) was used to analyze the mirror's reflectivity at tilt angles ranging from 15° to 45° in 5° increments (Figure 4.14). Based on this analysis, a 25° tilt was predicted to be optimal due to its selective reflectivity, reflecting the 266 nm excitation light while transmitting the fluorescence signal (emitted at slightly higher wavelengths).

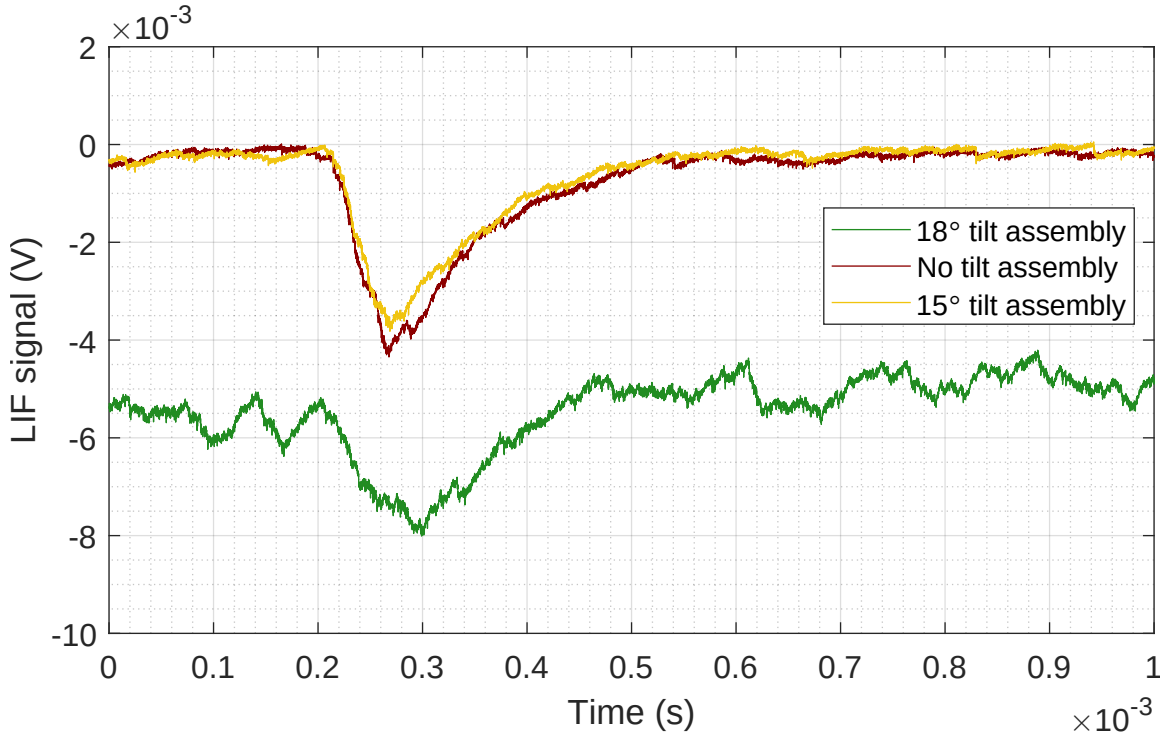

Fig. 4.15. Impact of mirror tilt on LIF signal and background noise. Signal traces for no tilt, ~15° tilt, and ~18° tilt assemblies are shown.

Due to mechanical constraints imposed by the ~6 mm mirror thickness, the maximum achievable mirror tilt angle was ~18°. However, even at this angle, a significant amount of scattered light still entered the detection system, resulting in increased background noise and a poorer signal-to-noise ratio, as shown in Figure 4.15. Further reducing the tilt to ~15°, as well as to a no-tilt configuration, yielded comparable results with reduced noise.

The mirror configuration with no tilt applied was chosen for subsequent high-resolution LIF spectral measurements to ensure consistency and reproducibility. Future work may explore custom coated mirrors or modified mirror assemblies to achieve the predicted optimal 25° tilt, potentially further enhancing the signal-to-noise ratio by minimizing scattered light.

4.3.3 High-resolution LIF spectrum

The rotationally resolved LIF spectrum of the 1-phenylethanol origin band, previously identified by REMPI, was acquired using a narrow-band CW laser. A scan over 108.90 GHz was performed with a 4.5 MHz step size, and single lines featured a 54 MHz FWHM linewidth. This linewidth, significantly broader than the natural linewidth of ~2 MHz,

indicates that Doppler broadening is the dominant factor affecting the observed spectral resolution.

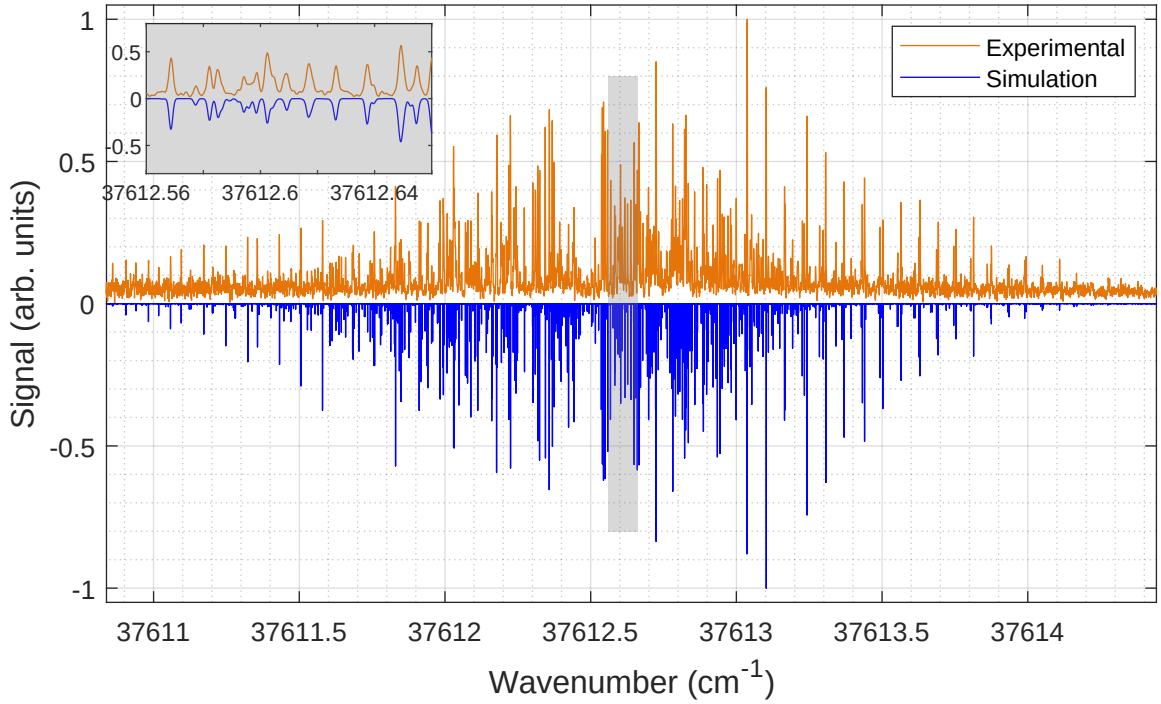

Fig. 4.16. High-resolution LIF spectrum and PGOPHER simulation for 1-phenylethanol. The inset highlights the excellent agreement between experimental and simulated spectrum.

Figure 4.16 shows the PGOPHER-fit and the experimental spectrum. The fitting process utilized theoretically predicted excited state rotational constants obtained in the Section 4.1.3 and literature-derived ground state constants.[11] Assignment of 419 spectral lines enabled an accurate fit, demonstrating excellent agreement with the experimental data (shown in orange), as highlighted by the inset in figure 4.16. The inset highlights several *R*-branch lines due to their importance in our optical pumping scheme used for ESST[7]. Notably, the first observed *R*-branch line appears at 37612.49 cm^{-1} and is assigned to the $7_{2,6}(S_1) \leftarrow 6_{3,3}(S_0)$ transition. The strongest signal, appearing at 37613.24 cm^{-1}, is assigned to the $4_{4,1}(S_1) \leftarrow 3_{3,0}(S_0)$ transition.

Analysis of the fitted spectrum also revealed a predominantly *b*-type character, with *a*-type and *c*-type transitions also present (intensity ratio $a : b : c = 0.6 : 1 : 0.07$). The rotationless electronic origin was determined to be 37612.45847(1) cm^{-1}. Based on the spectral fit, the molecular beam temperature for LIF measurements was estimated to be ~1.8 *K*.

Spectral fitting yielded key molecular parameters for the excited state (S_1), summarized in Table 4.4. These include rotational constants, rotationless electronic origin, transition dipole moments, asymmetry parameter, and inertial defect. The spectral fit directly provided excited state parameters. For comparison, Table 4.4 also includes ground state rotational constants from previous microwave spectroscopy studies[11] and theoretical calcu-

lations.

Table 4.4
Molecular parameters for 1-phenylethanol in the ground and first electronically excited state. Ground state parameters were obtained from previous microwave spectroscopy studies[11], while excited state parameters were determined from the spectral fit in this work. Calculated values at the B3LYP-D3BJ/6-311++G(d,p) level of theory are included for comparison (details in Section 4.1.3). Note: The 1σ standard deviations in parentheses are in units of the last digit.

$S_1(\nu_0) \leftarrow S_0(\nu_0)$		
	Experimental	Calculations
Ground state		
A (MHz)	3465.5588(1)	3471.98
B (MHz)	1103.96187(5)	1099.67
C (MHz)	981.27316(6)	982.48
Δ (amu Å^2)	-88.59	-90.74
κ	-0.901	-0.905
Excited state		
T_{00} (cm^{-1})	37612.45847(1)	40139.42
ΔA (MHz)	-109.16(1)	-104.9
ΔB (MHz)	-9.55(1)	-1.7
ΔC (MHz)	-22.373(8)	-17.97
μ_a	0.051	0.05
μ_b	-0.086	-0.08
μ_c	-0.006	-0.007
Δ (amu Å^2)	-85.31	-86.4
κ	-0.886	-0.889

Upon electronic excitation, a decrease in all rotational constants is observed, particularly pronounced along the *a*- and *c*-axis, suggesting expansion of the phenyl ring. The close agreement between experimental and theoretically calculated rotational constants validates the use of *ab initio* structural calculations for interpreting these changes. This observed expansion aligns with a predicted increases in C-C bond lengths within the phenyl ring, likely arising from a π to π^* transition within the aromatic system.

The inertial defect, indicative of molecular planarity, decreases upon excitation from -88.59 in the ground state to -85.31 in the excited state, suggesting increased planarity. This change likely arises from predicted shifts in the $\angle C_3$-C_{12}-OH (approximately 54° to 50°) and the $\angle C_4$-C_3-C_{12}-C_{13} dihedral angle (approximately 120° to 95°), implying movement of the OH and CH_3 groups towards the phenyl ring. The asymmetry parameter also shifts from -0.901 (ground state) to -0.886 (excited state), further supporting a decrease in molecular asymmetry upon excitation.

The successful determination of rotational constants for the S_1 excited state establishes 1-phenylethanol as a suitable candidate for ESST studies.

CHAPTER 5

Conclusions

We conducted high-resolution UV spectroscopy of 1-phenylethanol using REMPI and LIF. Initially, a vibrationally resolved REMPI spectra of the $S_1 \leftarrow S_0$ electronic transition was obtained using a jet-cooled pulsed molecular beam. By comparing the experimental spectrum with theoretical one-photon absorption calculations, we successfully identified the origin band at approximately 37612 cm^{-1} and several vibrational features. Vibrational modes, such as the Φ-R torsion (1_0^1) at +48 cm^{-1} and the CH_3 torsion (3_0^1) at +199 cm^{-1} above the origin band, were tentatively assigned based on the theoretical predictions. However, discrepancies between the experimental results and theoretical predictions in the 250-400 cm^{-1} region above the origin band indicate the need for improved theoretical models to fully explain the observed vibrational features.

Moreover, we measured the lifetime of the S_1 state using a two-color REMPI scheme by varying the time delay between two pulsed lasers. The lifetime was determined to be approximately 70 ns, corresponding to a natural linewidth of approximately 2.2 MHz. Given that the linewidth of the UV laser used for LIF is less than 1 MHz, this natural linewidth confirmed the feasibility of employing high-resolution LIF spectroscopy to resolve individual rotational transitions.

Following the REMPI results, we acquired a rotationally resolved LIF spectrum of the origin band of the $S_1 \leftarrow S_0$ electronic transition. The observed linewidth of 54 MHz suggests that Doppler broadening is the dominant factor limiting the spectral resolution, as the natural linewidth is considerably narrower. We analyzed the LIF spectrum using PGOPHER software, starting with known rotational constants for the S_0 ground state and calculated constants for the S_1 excited state. By systematically simulating the measured spectrum, we assigned all observed transitions in the fit, thereby determining the rotational energy level structure of the S_1 state.

We observed a decrease in rotational constants upon electronic excitation, particularly along the *a*- and *c*-axes. This indicates an expansion of the phenyl ring, likely due to a π to π^* transition within the aromatic system. The change in the inertial defect suggests increased

planarity in the excited state, with the OH and CH_3 groups moving towards the phenyl ring.

The successful determination of the S_1 state rotational constants for 1-phenylethanol completes the necessary criteria for it to be a suitable candidate for future ESST studies. Additionally, the measured 70 ns lifetime of the excited state further indicates its suitability for our ESST research, where depletion of one rotational state through optical pumping to the electronically excited state is crucial. Even if some molecules return to the original state upon UV excitation, the short lifetime of this state allows for more efficient optical cycles within the typical interaction time of around 5 μs.

Bibliography

1. Keszthelyi, L. Origin of the homochirality of biomolecules. *Quarterly reviews of biophysics* **28,** 473–507 1995.
2. Vargesson, N. Thalidomide-induced teratogenesis: History and mechanisms. *Birth Defects Research Part C: Embryo Today: Reviews* **105,** 140–156 2015.
3. Eibenberger, S., Doyle, J. & Patterson, D. Enantiomer-specific state transfer of chiral molecules. *Physical review letters* **118,** 123002 2017.
4. Lehmann, K. K. Influence of spatial degeneracy on rotational spectroscopy: Three-wave mixing and enantiomeric state separation of chiral molecules. *The Journal of Chemical Physics* **149** 2018.
5. Leibscher, M., Pozzoli, E., Pérez, C., Schnell, M., Sigalotti, M., Boscain, U. & Koch, C. P. Full quantum control of enantiomer-selective state transfer in chiral molecules despite degeneracy. *Communications Physics* **5,** 110 2022.
6. Zhang, Q., Chen, Y.-Y., Ye, C. & Li, Y. Evading thermal population influence on enantiomeric-specific state transfer based on a cyclic three-level system via ro-vibrational transitions. *Journal of Physics B: Atomic, Molecular and Optical Physics* **53,** 235103 2020.
7. Lee, J., Bischoff, J., Hernandez-Castillo, A. O., Sartakov, B., Meijer, G. & Eibenberger-Arias, S. Quantitative study of enantiomer-specific state transfer. *Physical Review Letters* **128,** 173001 2022.
8. Lee, J., Bischoff, J., Hernandez-Castillo, A., Abdiha, E., Sartakov, B., Meijer, G. & Eibenberger-Arias, S. The influence of microwave pulse conditions on enantiomer-specific state transfer. *New Journal of Physics* 2023.
9. Lee, J., Abdiha, E., Sartakov, B. G., Meijer, G. & Eibenberger-Arias, S. Full quantum state control of chiral molecules. *arXiv preprint arXiv:2402.17308* 2024.
10. Hirota, E. Triple resonance for a three-level system of a chiral molecule. *Proceedings of the Japan Academy, Series B* **88,** 120–128 2012.
11. Zheng, Y., Chen, J., Duan, C., Zhang, X., Xu, X. & Gou, Q. Accurate Geometry and Non-Covalent Interactions in 1-Phenylethanol and its Monohydrate: A Rotational Study. *ChemPhysChem* **24,** e202200804 2023.
12. Mandru, A., Mane, J. & Mandapati, R. A Review on UV-visible spectroscopy. *Journal of Pharma Insights and Research* **1,** 091–096 2023.

13. Eizner, E., Martınez-Martınez, L. A., Yuen-Zhou, J. & Kéna-Cohen, S. Inverting singlet and triplet excited states using strong light-matter coupling. *Science advances* **5,** eaax4482 2019.

14. Sutcliffe, B. T. in *Methods in Computational Molecular Physics* 19–46 Springer, 1992.

15. Zare, R. N. & Harter, W. G. Angular momentum: understanding spatial aspects in chemistry and physics. *New York* **120** 1988.

16. Hollas, J. M. *Modern spectroscopy* John Wiley & Sons, 2004.

17. Bernath, P. F. *Spectra of atoms and molecules* Oxford university press, 2020.

18. Arenas, B. E. High-resolution broadband rotational spectroscopy and electrical discharge experiments of astrochemically relevant molecules. 2020.

19. Zimmermann, R. Photo ionisation in mass spectrometry: light, selectivity and molecular ions. *Analytical and bioanalytical chemistry* **405,** 6901–6905 2013.

20. Chin, S. Multiphoton ionization of molecules. *Physical Review A* **4,** 992 1971.

21. Antonov, V., Knyazev, I., Letokhov, V. S., Matiuk, V., Movshev, V. & Potapov, V. Stepwise laser photoionization of molecules in a mass spectrometer: a new method for probing and detection of polyatomic molecules. *Optics Letters* **3,** 37–39 1978.

22. Ashfold, M. & Howe, J. Multiphoton spectroscopy of molecular species. *Annual Review of Physical Chemistry* **45,** 57–82 1994.

23. Gupta, V.. Principles and Applications of Quantum Chemistry. ed Gupta, V. , 155–194. Boston, Academic Press, 2016.

24. Hohenberg, P. & Kohn, W. Inhomogeneous electron gas. *Physical review* **136,** B864 1964.

25. Epstein, S. & Rosenthal, C. The Hohenberg–Kohn theorem. *The Journal of Chemical Physics* **64,** 247–249 1976.

26. Pople, J. A., Gill, P. M. & Johnson, B. G. Kohn—Sham density-functional theory within a finite basis set. *Chemical physics letters* **199,** 557–560 1992.

27. Perdew, J. P. & Wang, Y. Accurate and simple analytic representation of the electron-gas correlation energy. *Physical review B* **45,** 13244 1992.

28. Grimme, S. Semiempirical GGA-type density functional constructed with a long-range dispersion correction. *Journal of computational chemistry* **27,** 1787–1799 2006.

29. Andersson, M. P. & Uvdal, P. New scale factors for harmonic vibrational frequencies using the B3LYP density functional method with the triple-ζ basis set 6-311+ G (d, p). *The Journal of Physical Chemistry A* **109,** 2937–2941 2005.

30. Jacquemin, D., Mennucci, B. & Adamo, C. Excited-state calculations with TD-DFT: from benchmarks to simulations in complex environments. *Physical chemistry chemical physics* **13,** 16987–16998 2011.

31. Runge, E. & Gross, E. K. Density-functional theory for time-dependent systems. *Physical review letters* **52,** 997 1984.

32. Baer, R. & Kronik, L. Time-dependent generalized Kohn–Sham theory. *The European Physical Journal B* **91,** 1–9 2018.

33. Casida, M. E. TDDFT for excited states. *Computational Methods in Catalysis and Materials Science: An Introduction for Scientists and Engineers,* 33–59 2009.

34. Bagayoko, D. Understanding density functional theory (DFT) and completing it in practice. *AIP Advances* **4** 2014.

35. Frisch, A. *et al.* gaussian 09W Reference. *Wallingford, USA, 25p* **470** 2009.

36. Garcıa-Valverde, M., Cordero, N. & de la Cal, E. S. *GAUSSVIEW® as a tool for learning organic chemistry* in *EDULEARN15 Proceedings* 2015, 4366–4370.

37. Hernandez-Castillo, A. O., Bischoff, J., Lee, J. H., Langenhan, J., Karra, M., Meijer, G. & Eibenberger-Arias, S. High-resolution UV spectroscopy of 1-indanol. *Physical Chemistry Chemical Physics* **23,** 7048–7056 2021.

38. Western, C. PGOPHER 6.0, a Program for Simulating Rotational Structure; 2012; pgopher. chm. bris. ac. uk. *Google Scholar There is no corresponding record for this reference.*

39. Guidoni, A. G., Piccirillo, S., Scuderi, D., Satta, M., Di Palma, T. & Speranza, M. Chirality and intermolecular forces: studies using R2PI experiments in supersonic beams. *Physical Chemistry Chemical Physics* **2,** 4139–4142 2000.

40. Le Barbu, K., Lahmani, F., Mons, M., Broquier, M. & Zehnacker, A. IR–UV investigation of the structure of the 1-phenylethanol chromophore and its hydrated complexes. *Physical Chemistry Chemical Physics* **3,** 4684–4688 2001.

41. Verma, P., Wang, B., Fernandez, L. E. & Truhlar, D. G. Physical molecular mechanics method for damped dispersion. *The Journal of Physical Chemistry A* **121,** 2855–2862 2017.

42. Santoro, F. & Jacquemin, D. Going beyond the vertical approximation with time-dependent density functional theory. *Wiley Interdisciplinary Reviews: Computational Molecular Science* **6,** 460–486 2016.

43. Nibbering, N. & De Boer, T. J. Mass spectometry of aralkyl compounds with a functional group—VI1: Mass spectra of 1-phenylethyanol-1, 2-phenylethanol-1 and 1-phenylpropanol-2. *Organic Mass Spectrometry* **1,** 365–390 1968.

44. Lepelmeier, J., Alonso-Gómez, J. L., Mortaheb, F., Boesl, U., Heiz, U. & Kartouzian, A. Chiroptical inversion for isolated vibronic transitions of supersonic beam-cooled molecules. *Physical Chemistry Chemical Physics* **19,** 21297–21303 2017.

45. Santoro, F., Mortaheb, F., Lepelmeier, J., Boesl, U., Heiz, U. & Kartouzian, A. High-resolution absorption and electronic circular dichroism spectra of (R)-(+)-1-phenylethanol. Confident interpretation based on the synergy between experiments and computations. *ChemPhysChem* **19,** 715–723 2018.

46. Shin-ya, K., Sugeta, H., Shin, S., Hamada, Y., Katsumoto, Y. & Ohno, K. Absolute configuration and conformation analysis of 1-phenylethanol by matrix-isolation infrared and vibrational circular dichroism spectroscopy combined with density functional theory calculation. *The Journal of Physical Chemistry A* **111,** 8598–8605 2007.